

Joint Center for Satellite Data Assimilation

Office Note (unassigned)

THIS IS AN UNREVIEWED MANUSCRIPT, PRIMARILY INTENDED FOR INFORMAL
EXCHANGE OF INFORMATION AMONG JCSDA RESEARCHERS

CRTM: ATMS NPP Spectral Response Function Analysis

P. van Delst^a, D.N. Groff^b
JCSDA/EMC/SAIC

W.J. Blackwell^c
Massachusetts Institute of Technology

C.L. Chidester^d
Space Dynamics Laboratory, Utah State University

G. De Amici^e
Northrop Grumman Aerospace Systems

S. Swadley^f
Naval Research Laboratory

July, 2009

^apaul.vandelst@noaa.gov

^bdavid.groff@noaa.gov

^cwjb@mit.edu

^dLynn.Chidester@sdl.usu.edu

^egiovanni.deamici@ngc.com

^fsteve.swadley@nrlmry.navy.mil

Change History

Date	Author	Change
2009-07-16	P. van Delst	Initial release.

1 Introduction

Typically, when preparing the CRTM for microwave sensors, the only available channel frequency data consists of central frequencies (f_0), sideband offsets (df_1, df_2), and channel bandwidths (Δf). We start with the instrument specification of those quantities and later, once the instrument has been built and undergone testing, we end up with measured values for those quantities.

In generating CRTM coefficients, these frequency values are used to construct “boxcar” frequency responses. These boxcar responses are then used in the convolution of monochromatic quantities such as Planck radiances or transmittances to produce such things as polychromatic correction coefficients and instrument resolution transmittances. The latter are then regressed against a set of predictors to produce the fast transmittance model coefficients used by the CRTM.

DRAFT

2 ATMS Response Data

2.1 Specified and measured responses

The NPP ATMS specified central frequencies, sideband offsets and channel bandwidths, taken from table 9 of the CrIS EDR ATBD[2], are shown in table 2.1. Also shown are measured bandwidths taken from table 12-1 of the ATMS PFM Calibration Data Book[1]. No measurements of the central frequencies are readily available ¹.

Channel	Central Frequency ^a f_0 (GHz)	Sideband 1 Offset ^a df_1 (GHz)	Sideband 2 Offset ^a df_2 (GHz)	Specified Bandwidth ^a Δf (GHz)	Measured Bandwidth ^b Δf (GHz)
1	23.800000	-	-	0.27	0.258
2	31.400000	-	-	0.18	0.172
3	50.300000	-	-	0.18	0.173
4	51.760000	-	-	0.40	0.381
5	52.800000	-	-	0.40	0.366
6	53.596000	0.115	-	0.17	0.1587,0.1648 ^c
7	54.400000	-	-	0.40	0.387
8	54.940000	-	-	0.40	0.387
9	55.500000	-	-	0.33	0.317
10	57.290344	-	-	0.33	0.151
11	57.290344	0.217	-	0.078	0.0763
12	57.290344	0.3222	0.048	0.036	0.0351
13	57.290344	0.3222	0.022	0.016	0.01547
14	57.290344	0.3222	0.010	0.008	0.0078,0.0079 ^c
15	57.290344	0.3222	0.0045	0.003	0.0029
16	88.200000	-	-	2.0	1.9282
17	165.500000	-	-	3.0	1.1251
18	183.310000	7.0	-	2.0	1.9302
19	183.310000	4.5	-	2.0	1.9519
20	183.310000	3.0	-	1.0	0.9799
21	183.310000	1.8	-	1.0	0.9823
22	183.310000	1.0	-	0.5	0.4940

Table 2.1: Central, sideband offset, and bandwidth frequencies for ATMS. ^aData from table 9 of ref.[2].

^bData from table 12-1 of ref.[1]. ^cDifferent lower and upper sideband widths reported.

In addition to the usual frequency parameters, the ATMS PFM Calibration Data Book[1] contains tables (12-2a to 12-2d) of the digitised filter responses (hereafter referred to as the spectral response functions, or SRFs). Apart from channels 1 and 2, these digitised SRFs are at the intermediate frequencies (IF) at which the measurements were made, not at the actual on-orbit channel frequencies. So, these IF SRFs need to be processed so as to represent the SRFs at the frequencies corresponding to the on-orbit channel radiance measurements. The procedures used to do this for the “Table 12” IF SRF are shown schematically in figure 2.1. Two operations are performed: translation and reflection; how they are carried out depends on the ATMS channel:

Single Passband Channels, fig.2.1(a). Channels 3-5,7-10,16,17. The measured IF SRFs are simply translated to the channel central frequency, f_0 . The value of the IF central frequency, $f_{i,0}$, is obtained from the first moment of the SRF.

Double Sideband Channels, fig.2.1(b). Channels 11, 18-22. Here a single measured IF sideband is reflected about 0GHz (corresponding to $f_{i,0}$ in this case) and the two sidebands are then translated to the channel central frequency, f_0 .

¹These values may be available in other ATMS reports, particularly: RE-13680 K/Ka Band Receiver Shelf Verification Report, RE-13658 W Band Receiver Shelf Verification Report, RE-13741 V Band Receiver Shelf Verification Report, and RE-13802 G Band Receiver Shelf Verification Report.

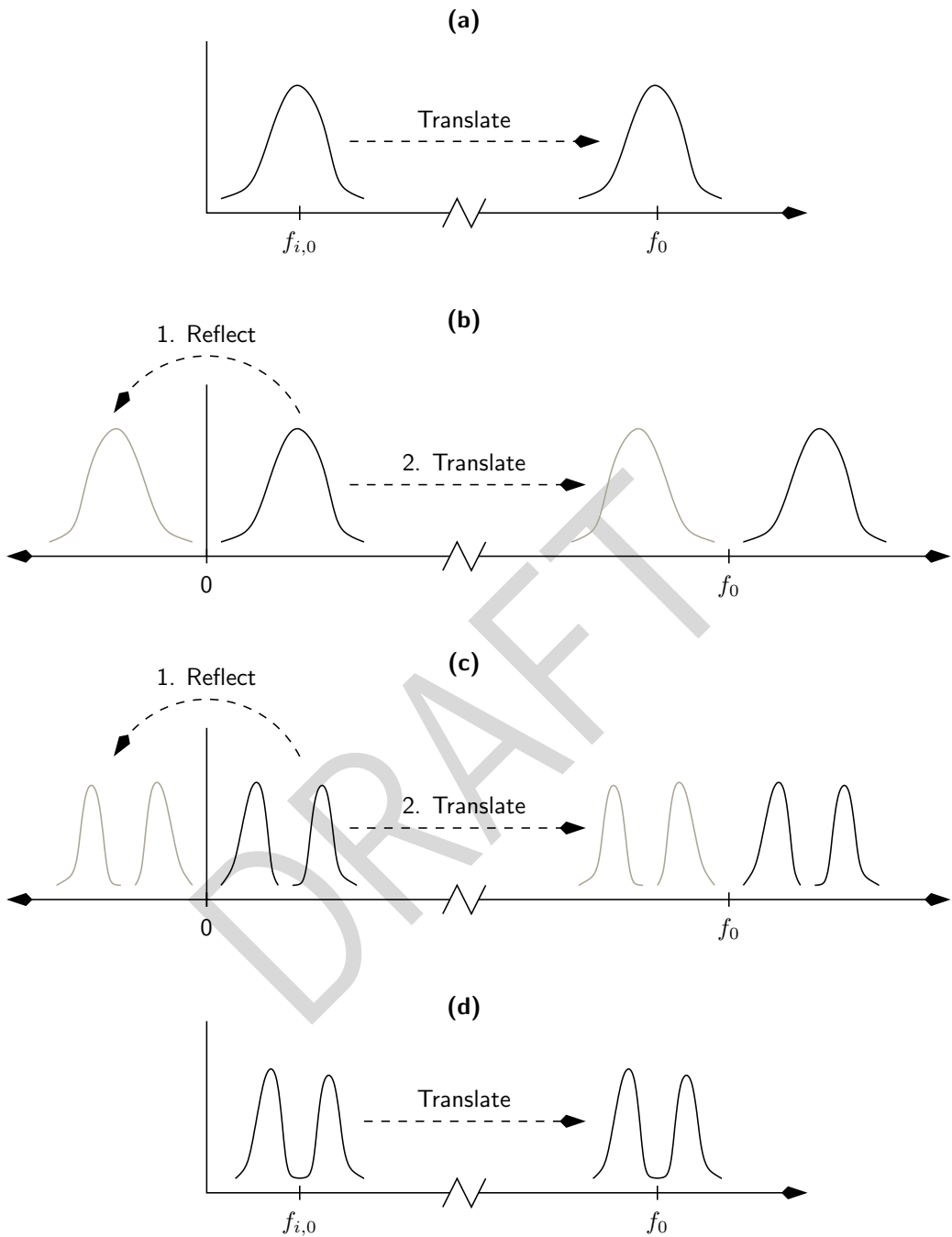


Figure 2.1: Schematic illustration of how the ATMS responses, measured at intermediate frequencies, were processed to SRFs at the measurement frequencies. **(a)** Single passband channels (3-5, 7-10, 16, 17). **(b)** Double passband channels (11, 18-22). **(c)** Quadruple passband channels (12-15). **(d)** Channel 6.

Quadruple Sideband Channels, fig.2.1(c). Channels 12-15. In this case two non-contiguous sidebands are reflected about 0GHz (again, corresponding to $f_{i,0}$) and all four sidebands are then translated to the channel central frequency.

Channel 6, fig.2.1(d). This channel is mentioned separately since, while it is a double sideband channel, unlike the other double sideband channels the IF SRF data contains the contiguous measurement of both sidebands. Thus only translation is applied to the IR SRF. As with the single passband channels, the IF central frequency is the first moment of the SRF. Note that this leads to a different bandwidth for the two sidebands; a situation one doesn't get for for the typical case in fig. 2.1(b). It does beg the question as to why the same procedure wasn't performed for the other multi-band channels.

A selection of four channels from the Table 12 ATMS SRF data, compared to the boxcar response, are shown in figure 2.2. All of the channel SRF are shown in appendix A. Two channels were selected for display in figure 2.2 to highlight their significant difference from the boxcar response: channel 10 (fig.2.2(b)) because the spec. bandwidth is quite different from that measured by about a factor of two²; and channel 19 (fig.2.2(d)) because, while the measured data does cover the specified bandwidth, the in-band SRF magnitudes appear to decrease anomalously.

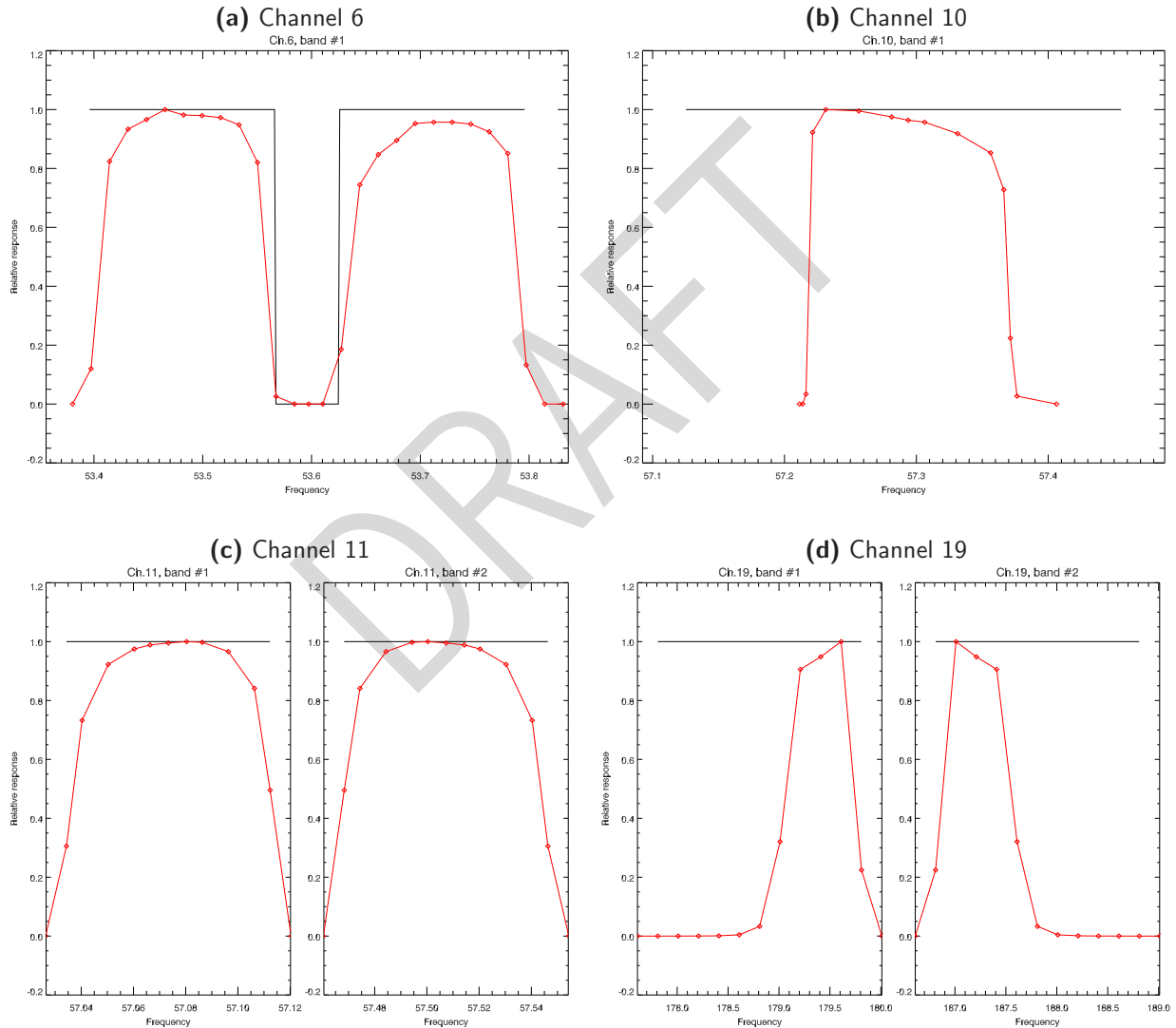


Figure 2.2: Selection of NPP ATMS Table 12 SRF data from reference [1] with the corresponding boxcar response based on table 2.1 data.

²Channel 17 suffers similarly; see figure A.17

2.2 Additional Digitised Responses

After a recent SOAT meeting³ where the NPP ATMS Table 12 SRF data was discussed, two of us (Chidester, SDL; and DeAmici, NGAS) separately digitised the graphical SRFs displayed in the ATMS PFM Calibration Data Book[1]. The SDL dataset consisted of channels 1, 12, 13, 14, and 15; and the NGAS dataset consisted of channels 4, 5, 9, 13, and 14. These digitised SRFs, along with the corresponding boxcar and Table 12 SRFs, are shown in figures 2.3 (single passband channels) and 2.4 (quadruple passband channels).

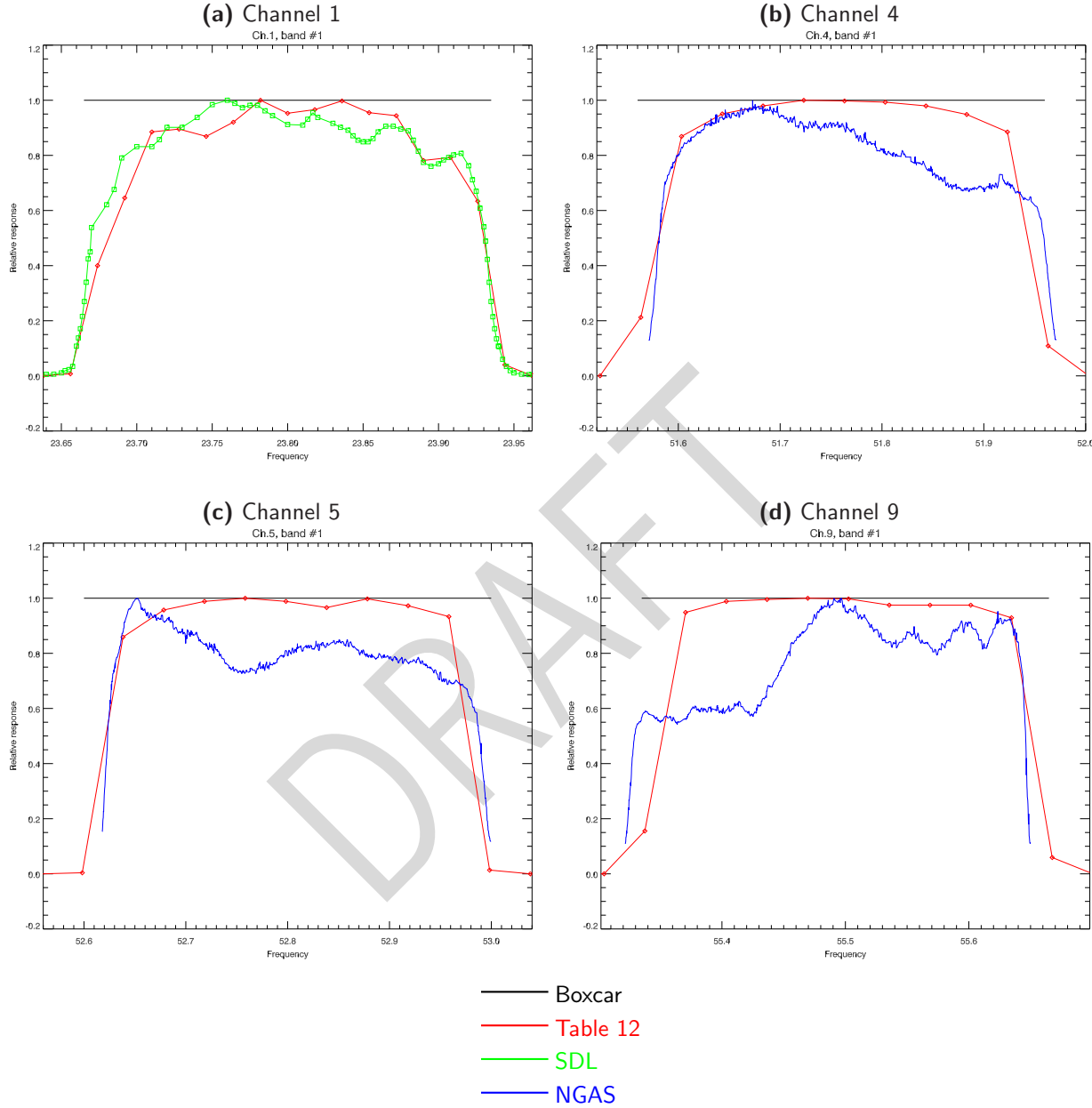


Figure 2.3: Single passband SDL and NGAS digitised NPP ATMS SRFs from reference [1] with the corresponding boxcar and Table 12 response

For the single passband channels shown in figure 2.3, the SDL channel 1 digitisation of fig.2.3(a) appears to be most like the Table 12 representation. For the NGAS digitisations, figs.2.3(b)-(d), the outstanding feature is how very different the digitised data is from the Table 12 data. Lest readers think the digitisation procedures somehow went awry, they are referred to Appendix A – in particular figures A.1, A.4, A.5, and A.9 – where the plots shown

³Sounding Operational Algorithm Team (SOAT) Meeting, CrIS/ATMS Cal/Val Team, Integrated Program Office, Silver Spring, Maryland, USA, 20-21 May 2009

in 2.3 are replicated at a larger size, but also with the corresponding filter response taken from the ATMS PFM Calibration Data Book [1]. Comparison of these plots clearly show that the SDL and NGAS digitisations are more representative of the measurements displayed in [1].

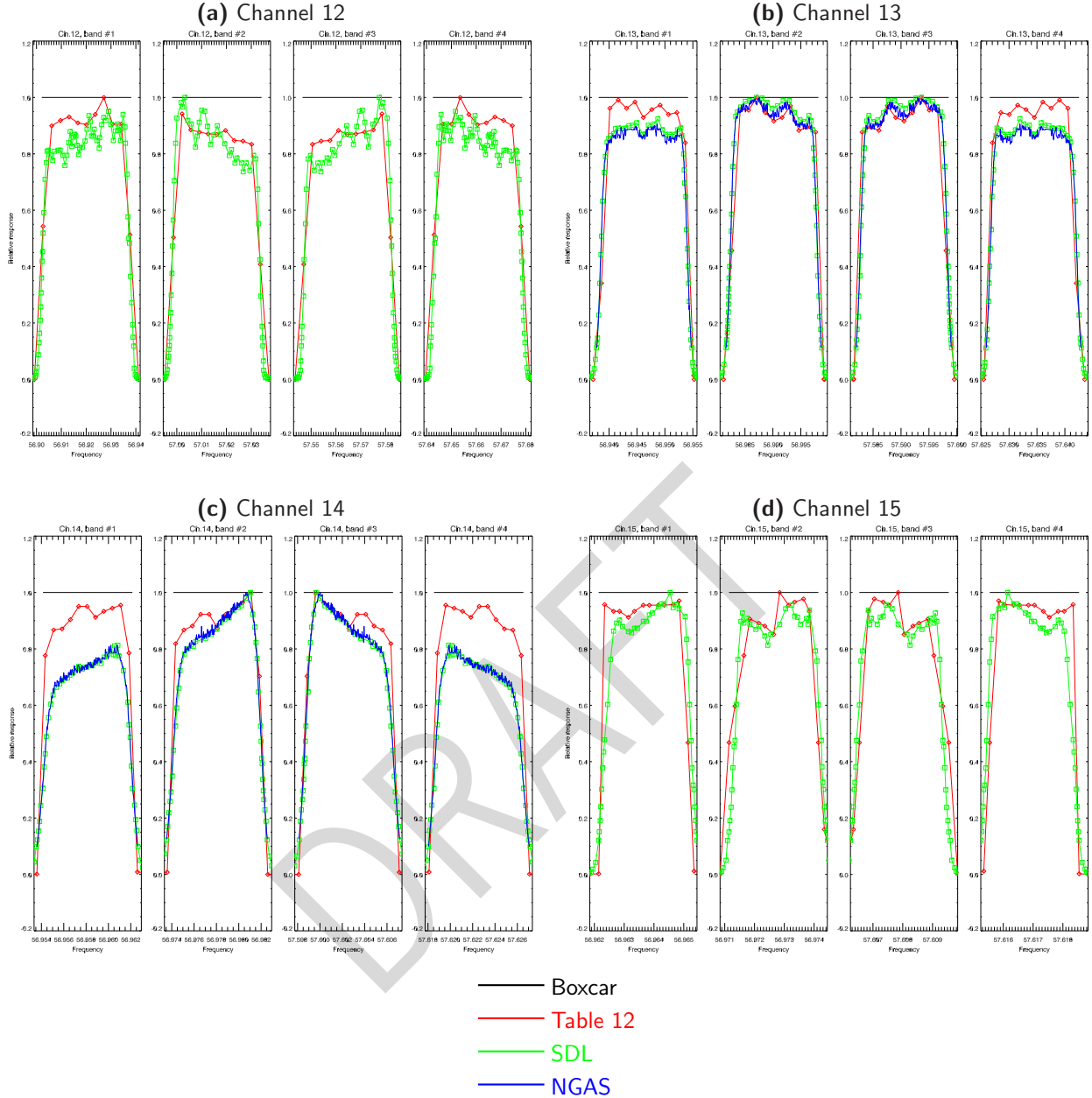


Figure 2.4: Quadrupole passband SDL and NGAS digitised NPP ATMS SRFs from reference [1] with the corresponding boxcar and Table 12 response

Similarly, for the quadrupole passband channels shown in figure 2.4, the SDL and NGAS digitisations are quite different from the Table 12 data. Of particular interest is the difference in relative magnitudes between the “inner” (#2 and #3) and “outer” (#1 and #4) bands for channels 13 and 14 in figs.2.4(b) and (c). Comparison of the digitised data with that displayed in the ATMS PFM Calibration Data Book [1] – see figures A.12, A.13, A.14, and A.14 – again shows the SDL and NGAS digitisation to be more representative of the filter responses, in both shape and relative magnitude, than the Table 12 data. It should be pointed out that the vertical excursions for the relative response plots are more pronounced than for those where the y-axis is signal loss with units of decibels.

3 Radiative Transfer Calculations

3.1 Methodology

Monochromatic radiative transfer calculations were done at the various tabulated ATMS SRF frequencies using MonoRTM [8, 5] and the ECMWF83 profile set [7, 3]. The subsequent spectra were then convolved with the tabulated SRFs using a simple numerical integration routine.

The temperature and water vapour from the ECMWF83 set are shown in figure 3.1 to provide an indication of the range of inputs. We realise 83 profiles is a small sample and are looking at repeating the calculations for a larger (1000's of profiles) data set.

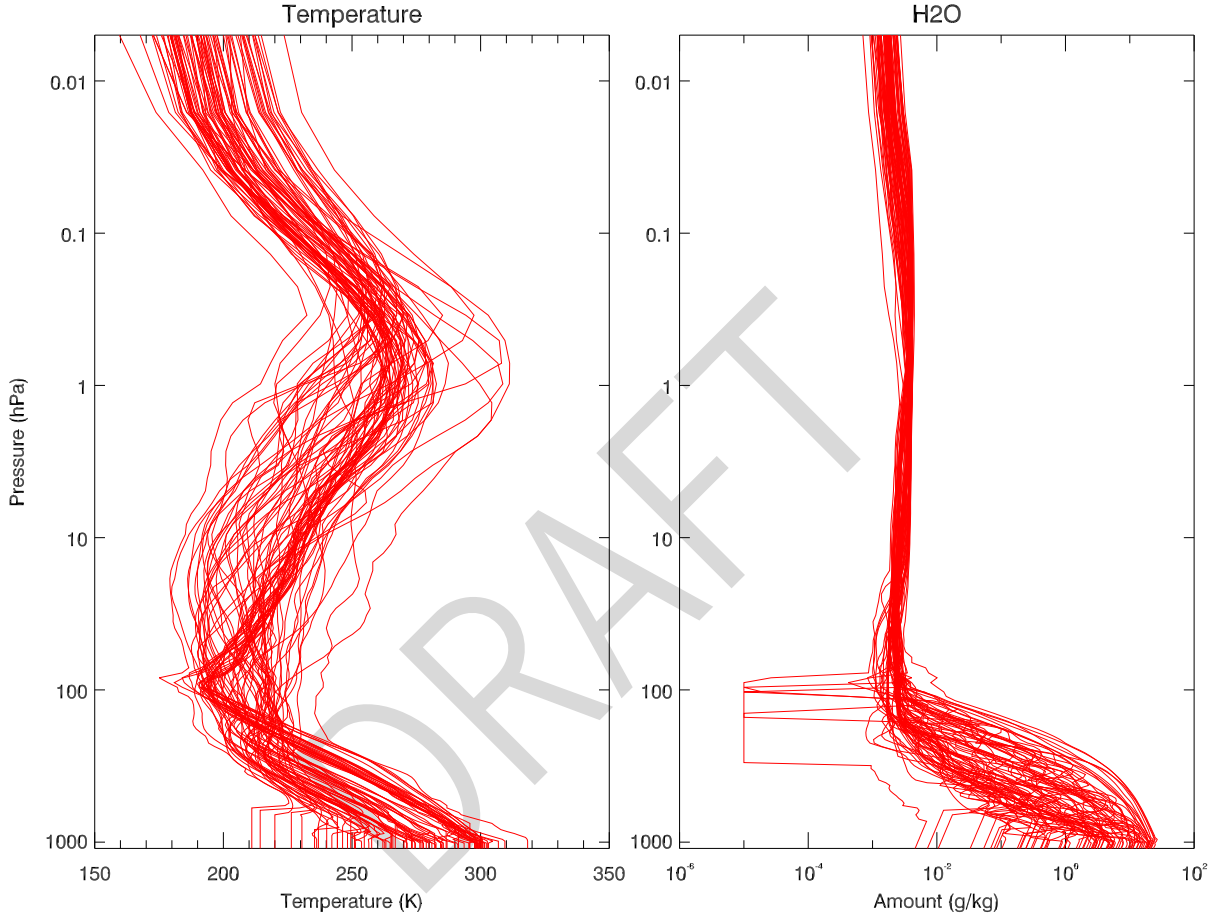


Figure 3.1: The temperature and water vapour profiles from the ECMWF83 profile dataset used in the radiative transfer calculations.

3.2 Results

The results for the different digitised, or measured, SRFs are presented here as brightness temperature differences from the boxcar SRF result, that is,

$$\Delta T_B = T_{B,Boxcar} - T_{B,Measured} \quad (3.1)$$

The ΔT_B values are displayed as a function of $T_{B,Boxcar}$ as well as a histogram of the differences. Only the results for those channels for which we have either SDL or NGAS digitised SRFs will be discussed here. Results for all the channels are shown in Appendix B. Since the reference for the brightness temperatures differences is the boxcar SRF, it should also be noted that these comparisons are intended to highlight the impact of the differences between the various digitised SRFs, not necessarily to indicate which is “better”.

3.2.1 Single passband channels: 1, 4, 5, and 9

The ΔT_B scatterplots for the single passband channels 1, 4, 5, and 9 are shown in figure 3.2, and the corresponding histograms are shown in figure 3.3. In all cases the SDL and NGAS digitisations decreased the ΔT_B values, although to different degrees.

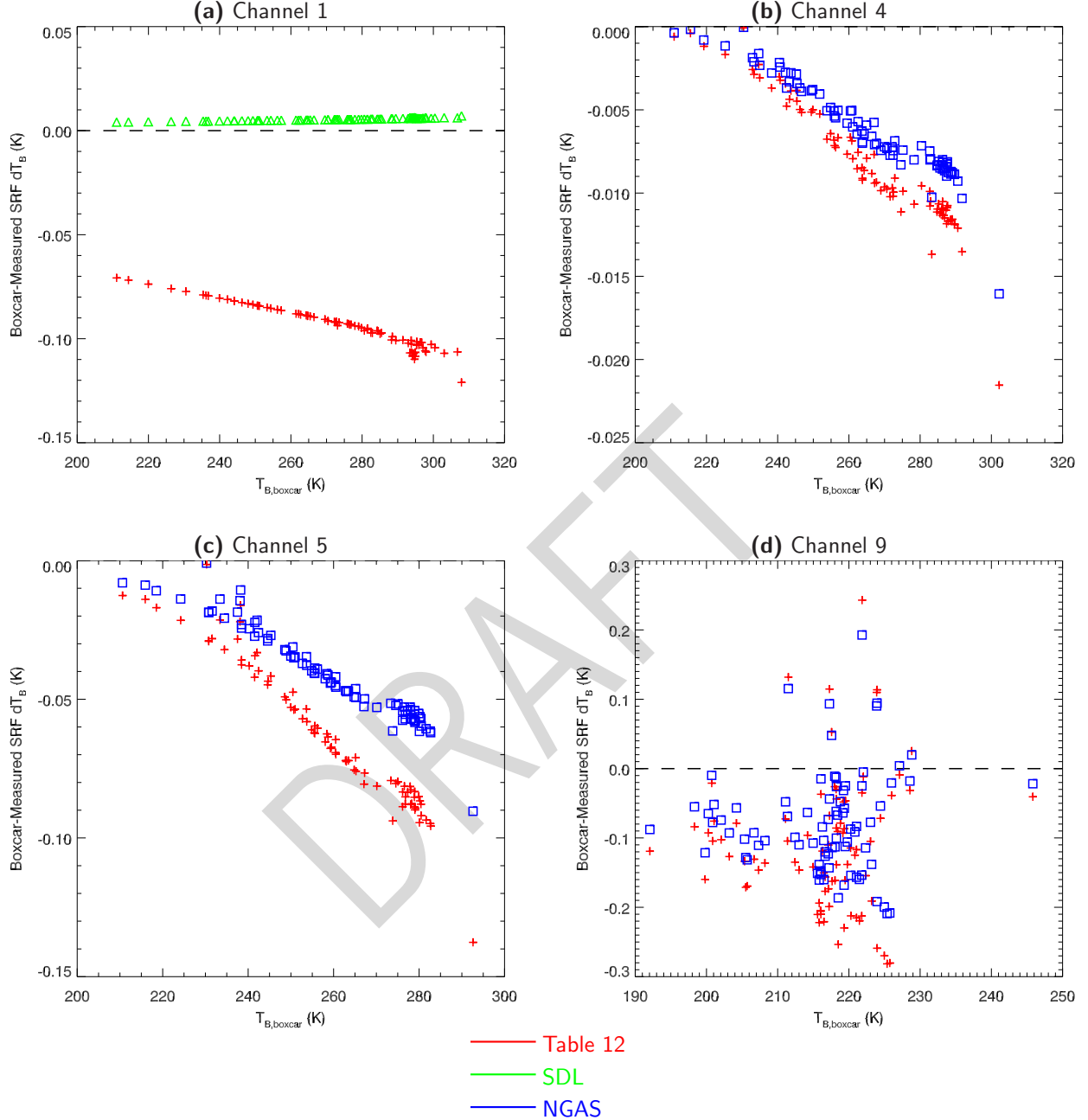


Figure 3.2: Scatterplots of the calculated brightness temperature differences, ΔT_B , as a function of the boxcar SRF $T_{B,Boxcar}$ for the single passband SDL and NGAS digitised SRFs

The most striking change is for channel 1 (figs.3.2(a) and 3.3(a)) where both the magnitude and spread of the differences decreased markedly with the SDL digitised SRF producing a result much closer to that of the boxcar response with little dependence on $T_{B,Boxcar}$. For channels 4 and 5 we have NGAS digitised SRF data and, despite the SRF differences being quite profound, the ΔT_B differences (figs.3.2(b),(c) and 3.3(b),(c)) do not really reflect this (at least, compared with the result for channel 1). The channel 9 radiometric differences (figs.3.2(d) and 3.3(d)) do not change too much between the Table 12 and NGAS SRF results despite the large differences in the SRF shape.

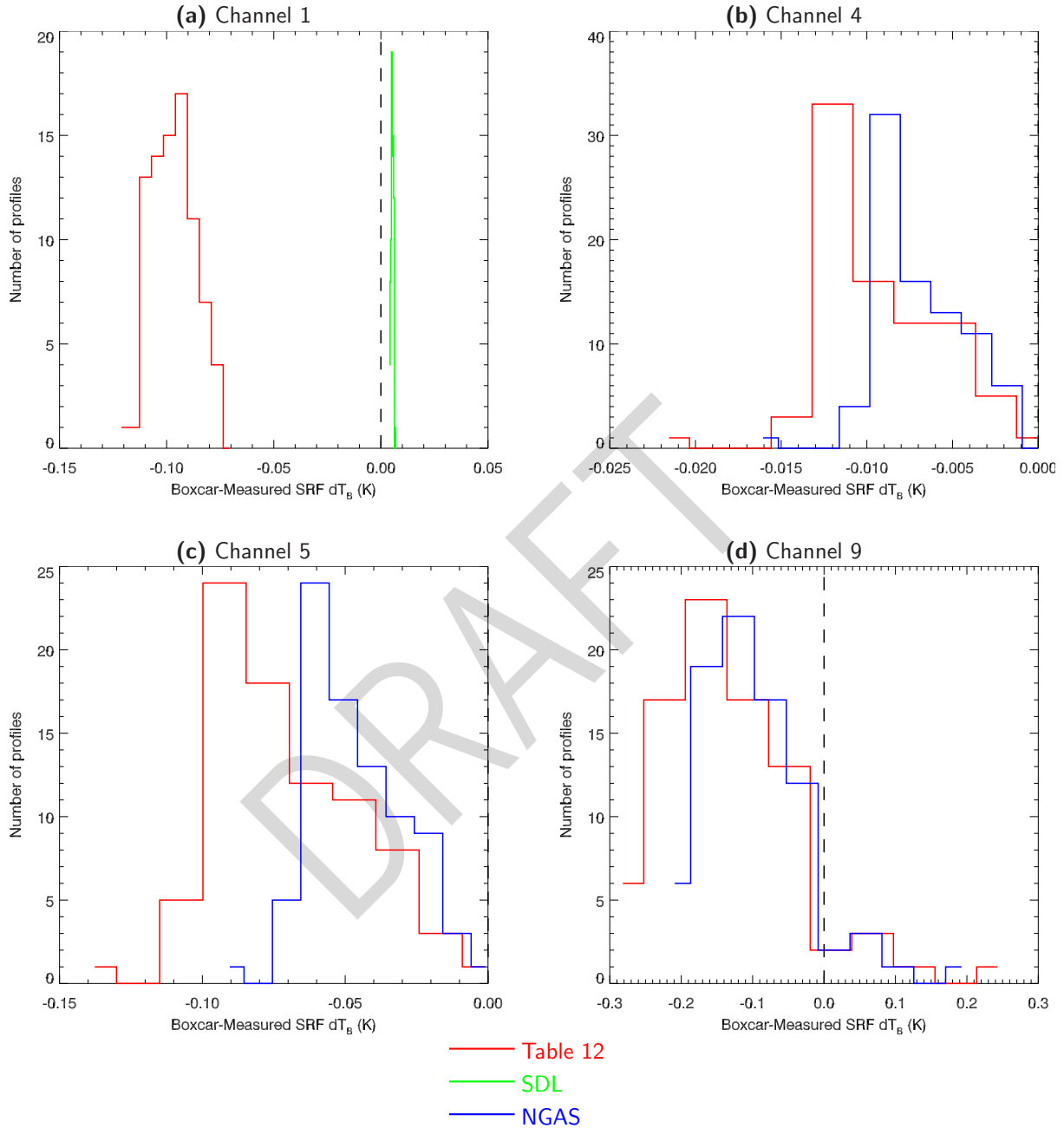


Figure 3.3: Histograms of the calculated brightness temperature differences, ΔT_B , for the single passband SDR and NGAS digitised SRFs.

To further determine the cause of the ΔT_B differences in these channels, spectra were generated for a single profile (tropical climatology) for the channel bandwidth. These spectra are shown in figure 3.4. Comparison of figure 3.4 with the SRFs shown in figure 2.3 do not yield any obvious cause. Specifically, for:

Channel 1: The shapes of the Table 12 and SDL SRFs are not *that* dissimilar. Furthermore, the variation of brightness temperature across the channel bandwidth is very small, $\sim 0.05\text{K}$. Looking closely at figure 2.3(a), the only SRF difference that could be construed to cause the brightness temperatures we see are the higher magnitudes of the SDL SRF on the low-frequency band edge at frequencies less than 23.70GHz.

Channel 4: Here we have an almost opposite effect compared to channel 1 in that the Table 12 and NGAS SRFs are very different, but the brightness temperatures not so much. There is a 1K variation across the channel spectrum of figure 3.4(b) and, somewhat similarly to channel 1, one could theorise that in this case the higher-frequency band edge of the NGAS SRF compensates for the much smaller in-band magnitudes.

Channel 5: The results here mirror those of channel 4 but with larger magnitudes most likely due to the larger 4K variation across the channel spectrum of figure 3.4(c).

Channel 9: Here we see a much larger ($\sim 6\text{K}$), but also very non-linear, variation across the channel spectrum of figure 3.4(d). Given the results for the Table 12 and NGAS SRF data (fig.2.3(d)) do not change much given the large SRF differences (fig.2.3(d)) viewing the in-band spectrum for a single profile does not yield too much insight.

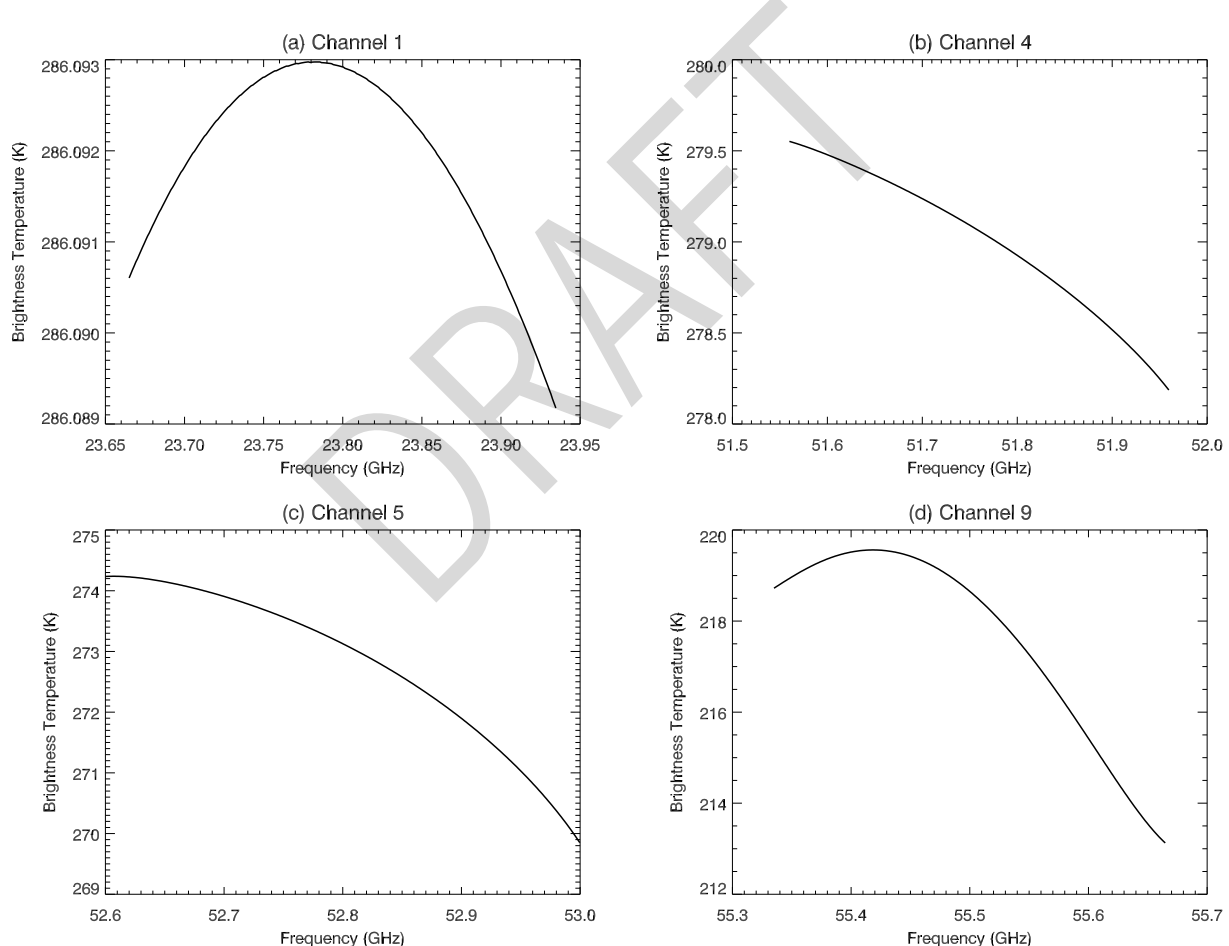


Figure 3.4: Spectra generated using MonoRTM for tropical climatology for the NPP ATMS single passband channels for which there exists SDL and NGAS digitised SRFs.

3.2.2 Quadruple passband channels: 12, 13, 14, and 15

The ΔT_B scatterplots for the quadruple passband channels 12, 13, 14, and 15 are shown in figure 3.5, and the corresponding histograms are shown in figure 3.6.

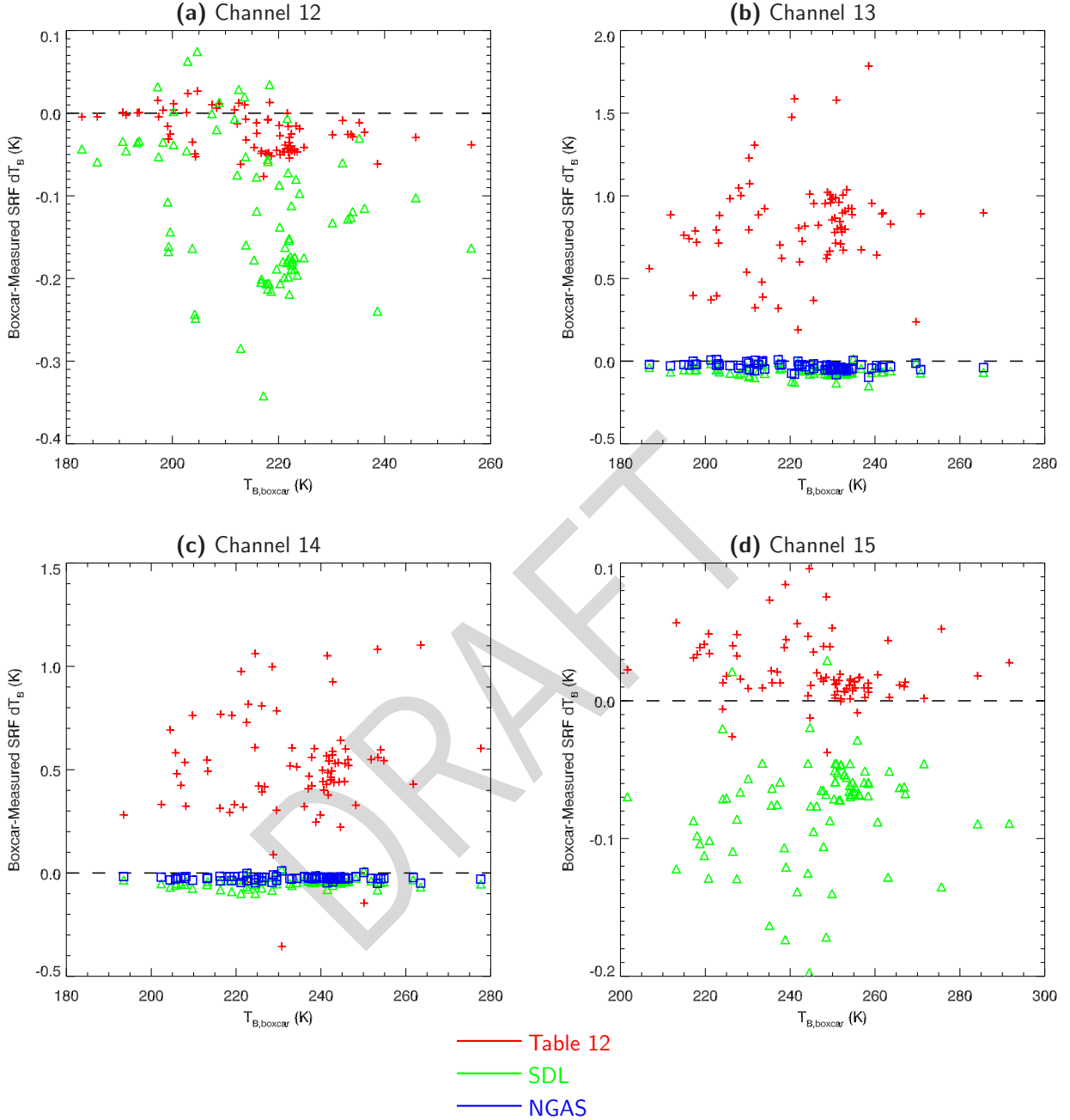


Figure 3.5: Scatterplots of the calculated brightness temperature differences, ΔT_B , as a function of the boxcar SRF $T_{B,Boxcar}$ for the quadruple passband SDL and NGAS digitised SRFs

The results group themselves into two categories: channels where the newly digitised SRFs decrease the ΔT_B values and their spread (channels 13 and 14, figs. 3.5(b),(c) and 3.6(b),(c)) and channels where the converse is true (channels 12 and 15, figs. 3.5(a),(d) and 3.6(a),(d)).

For the channel 13 and 14 case where the ΔT_B values decrease, we have both SDL and NGAS SRF data (see figs. 2.4(b) and (c)) which agree quite well, as do their respective ΔT_B results⁴. The most obvious difference between the

⁴This would indicate the digitisation methodologies employed are not contributing significantly to any differences

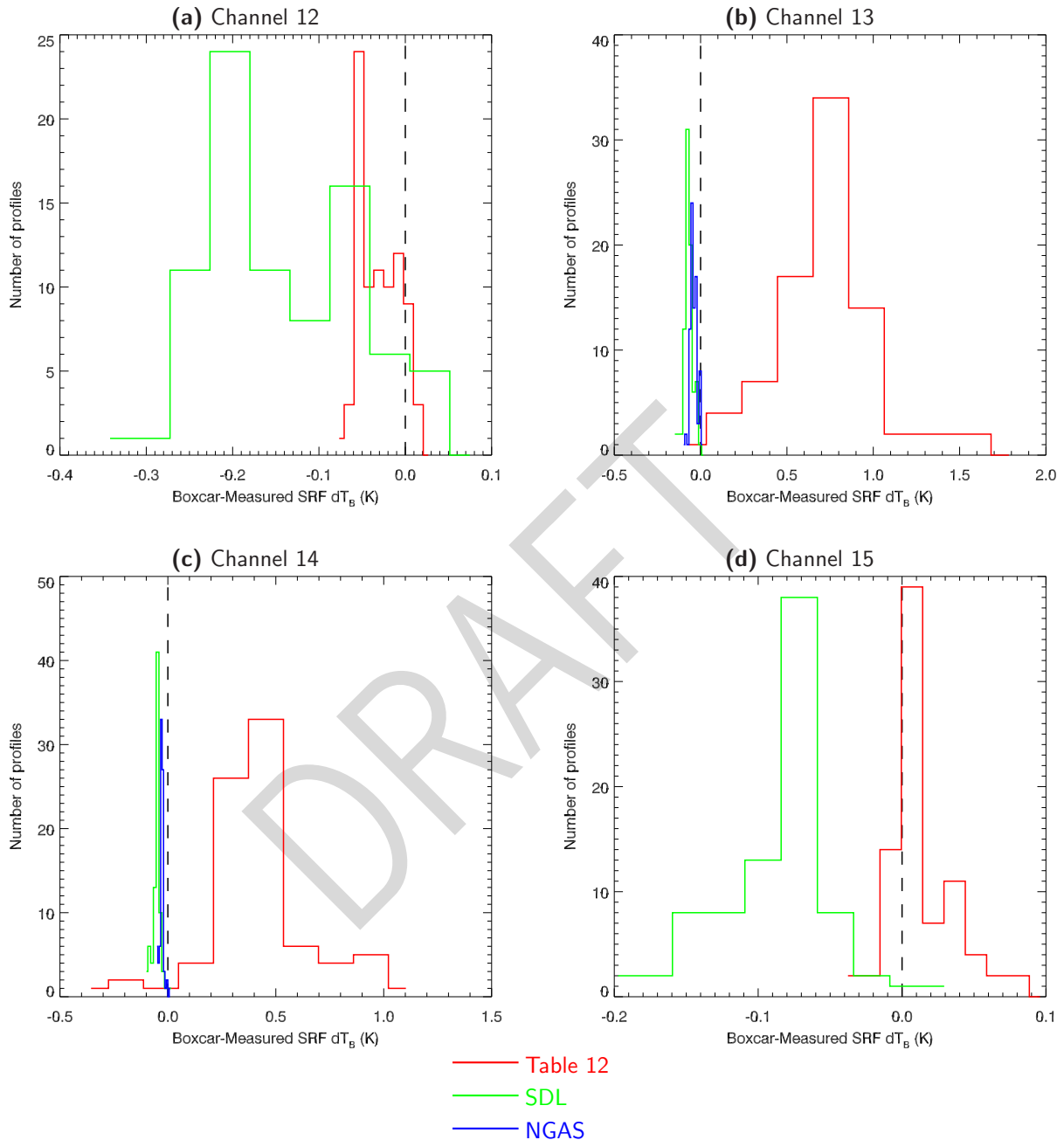


Figure 3.6: Histograms of the calculated brightness temperature differences, ΔT_B , for the quadruple passband SDL and NGAS digitised SRFs

SDL/NGAS and Table 12 SRFs is that for the former the relative magnitudes of the “outer” bands, #1 and #4, are about 10% less than that for the “inner” bands, #2 and #3. This is not seen in the Table 12 SRF data.

For channels 12 and 15, where we only have SDL SRF data to compare (fig.2.4(a) and (d)), the band relative magnitudes are fairly uniform but the impact of the SRF differences manifest themselves with a much larger bias and spread. Thus the SRF differences are obviously significant, but it’s not immediately clear from comparisons of figures 2.4 and 3.5 what feature of the SRF differences produces larger ΔT_B values.

As with the single passband channels, spectra were generated for a single profile (tropical climatology) for the channel bandwidths. These spectra are shown in figure 3.7 along with the a plot-spanning monochromatic spectrum for context. Even though the channel bandwidths and positions about the O₂ absorptions lines in question are different, the trend of the radiances across the channel bands are similar – e.g. the range of brightness temperature change across a band is about the same for all channels, ~ 10 K. Thus, figure 3.7 doesn’t really help reveal why the different SRFs of figure 2.4 produce the bipolar results seen in figures 3.5 and 3.6.

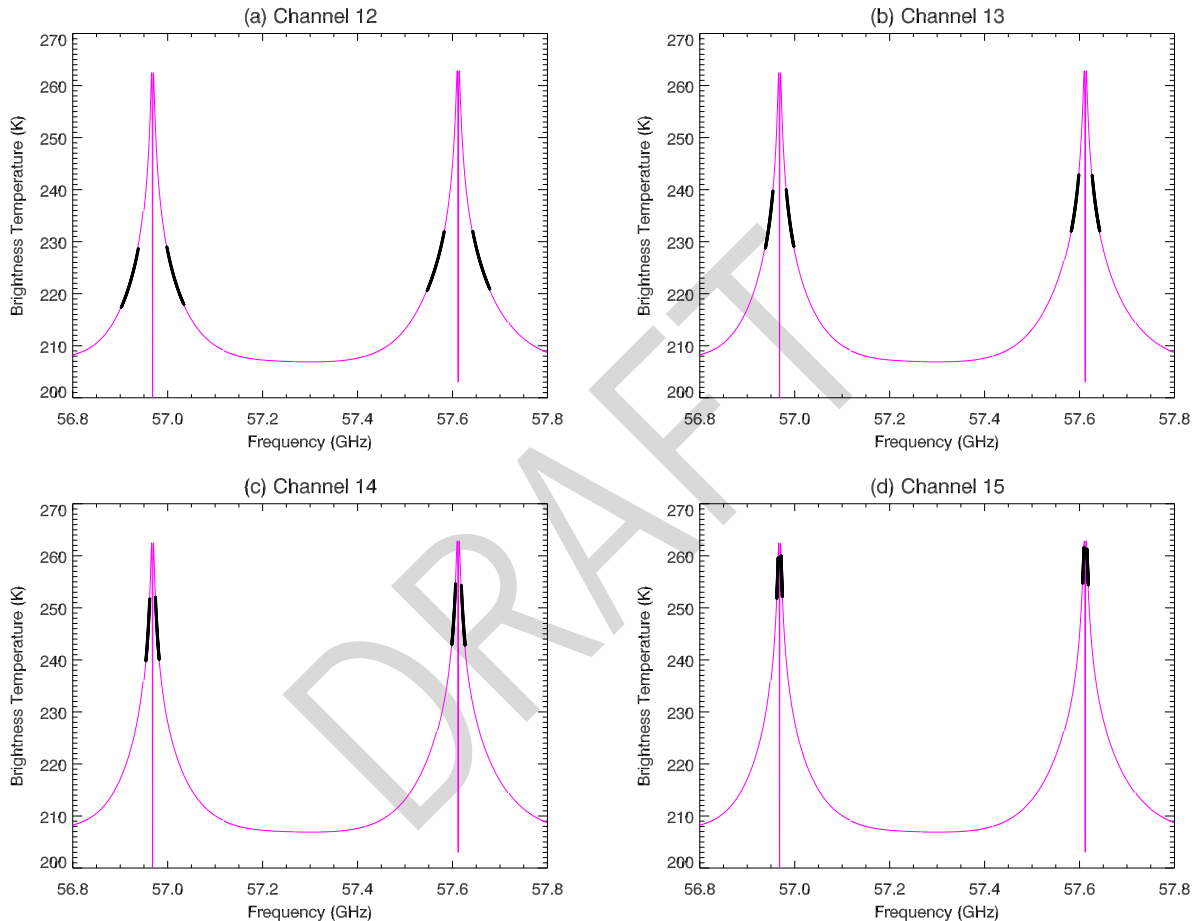


Figure 3.7: Spectra generated using MonoRTM for tropical climatology for the NPP ATMS quadruple passband channels for which there exists SDL and NGAS digitised SRFs. The portion of the spectrum to which the channels are sensitive are represented by the heavy black lines. The full spectrum (magenta coloured line) is there for context.

4 Conclusions

Four different ATMS SRFs were used in this study: a simple boxcar SRF derived using the passband widths and frequency offsets; digitised data taken from the ATMS PFM Calibration Data Book^[1], the “Table 12” SRFs; digitisations of selected channels from reference [1] performed at SDL, the “SDL” SRFs; and digitisations of selected channels from reference [1] performed at NGAS, the “NGAS” SRFs.

The degree to which the differences in the SRFs is reflected in the radiative transfer results of section 3 varies with the channel with no clear pattern.

Comparison of the common SDL and NGAS SRFs indicate that the digitisation process used is not a factor, although the quality of the figures from reference [1] that were used are a factor, as pointed out by both C.L. Chidester and G. DeAmici when they encountered non-orthogonal axes in the scanned figures.

While additional measurements of the NPP ATMS channel responses may no longer be possible, what should be required for future NPOESS ATMS instruments (indeed, any future microwave instrument) is the original digital data of the measured channel responses. This can only serve to mitigate lack of knowledge of the channel spectral response functions as a source of error in the on-orbit measured radiances.

DRAFT

References

- [1] Advanced Technology Microwave Sounder (ATMS) Calibration Data Book, ATMS PFM P/N 1362460-1 S/N 302. Contract No. NAS5-01089 CDRL 042 submitted to NASA-GSFC, October 2005.
- [2] Cross Track Infrared Sounder (CrIS) Volume 2, Environmental Data Records (EDR) Algorithm Theoretical Basis Document (ATBD). Contract No. F04701-02-C-0502, February 2007.
- [3] F. Chevallier, S. Di Michele, and A.P. McNally. Diverse profile datasets from the ECMWF 91-level short-range forecasts. NWP SAF Report NWPSAF-EC-TR-010.B, EUMETSAT/ECMWF, 2006.
- [4] C.L. Chidester. Private communication, 2009.
- [5] S.A. Clough, M.W. Shephard, E.J. Mlawer, J.S. Delamere, M.J. Iacono, K. Cady-Pereira, S. Boukabara, and P. D. Brown. Atmospheric radiative transfer modeling: a summary of the AER codes. *J. Quant. Spectrosc. Radiat. Transfer*, 91:233–244, 2005.
- [6] G. DeAmici. Private communication, 2009.
- [7] M. Matricardi. The generation of RTTOV regression coefficients for IASI and AIRS using a new profile training set and a new line-by-line database. ECMWF Technical Memorandum 564, ECMWF, May 2008.
- [8] V.H. Payne, J.S. Delamere, K.E. Cady-Pereira, R.R. Gamache, J-L. Moncet, E.J. Mlawer, and S.A. Clough. Air-broadened half-widths of the 22 and 183 GHz water vapor lines. *IEEE Trans. Geosci. Remote Sens.*, 46(11):3601–3617, 2008.

A ATMS NPP channel SRF comparisons

This appendix plots the various NPP ATMS microwave spectral response functions (SRFs) used in this study. The "boxcar" data is derived from the data shown in table 2.1, the "Table 12" data is an edited form of the data from table 12 in reference [1], and the SDL [4] and NGAS [6] data are digitisations of various measured ATMS channel response plots shown in reference [1].

DRAFT

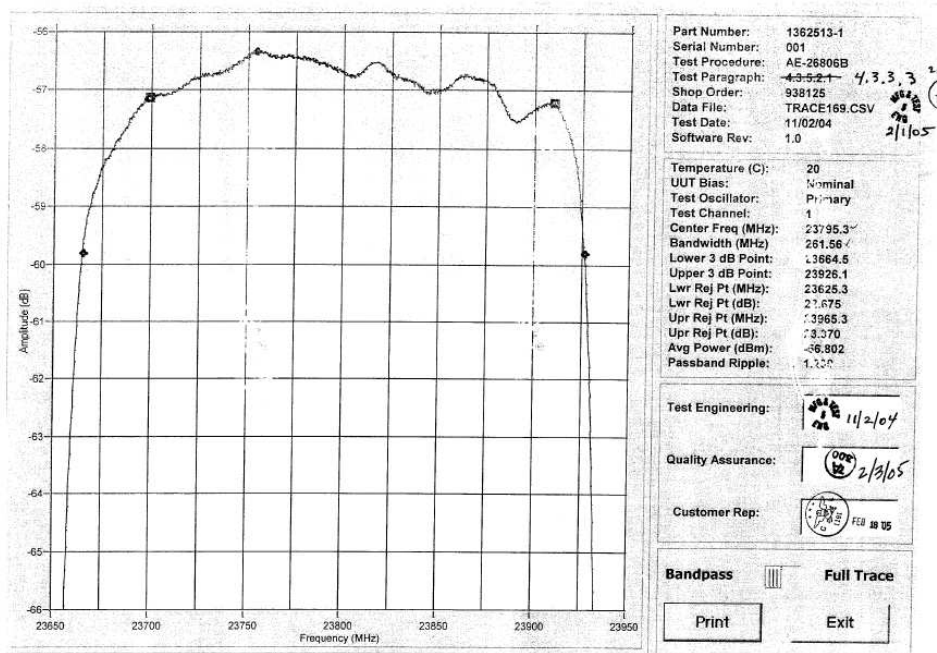
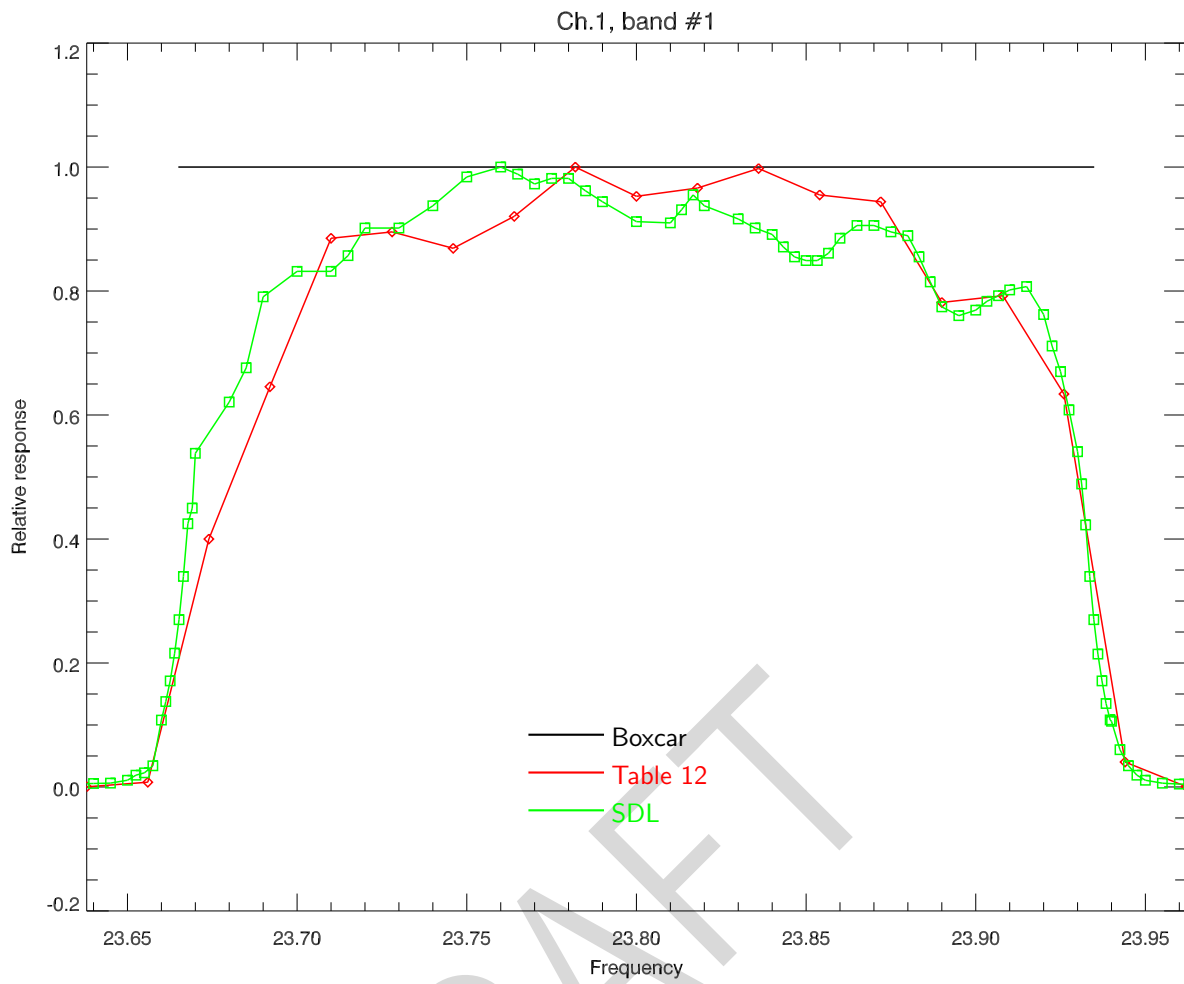


Figure A.1: NPP ATMS channel 1 response. (**Top**) Boxcar and digitised data. (**Bottom**) Nominal filter response from ATMS Calibration Data Book[1].

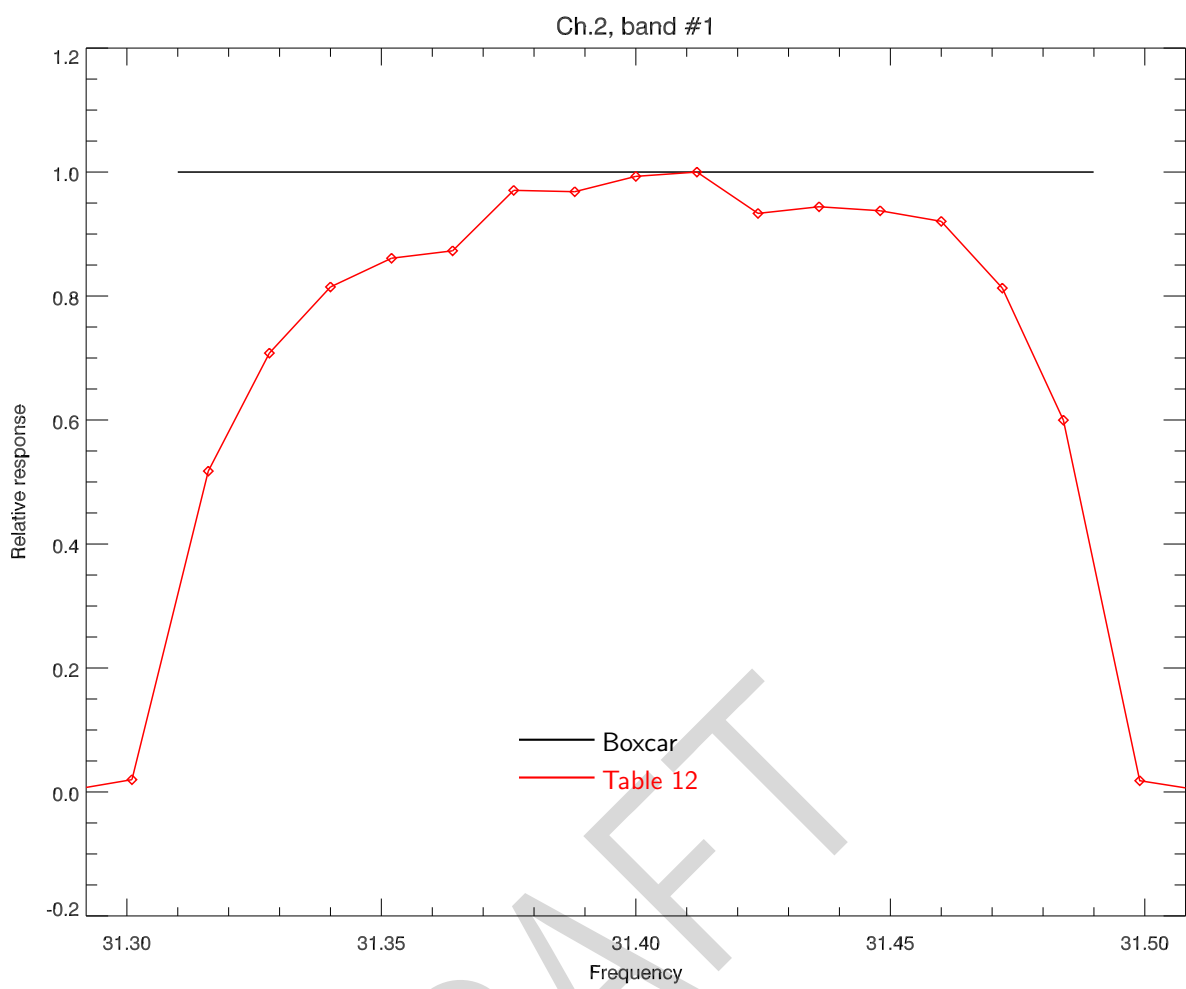


Figure A.2: NPP ATMS channel 2 response.

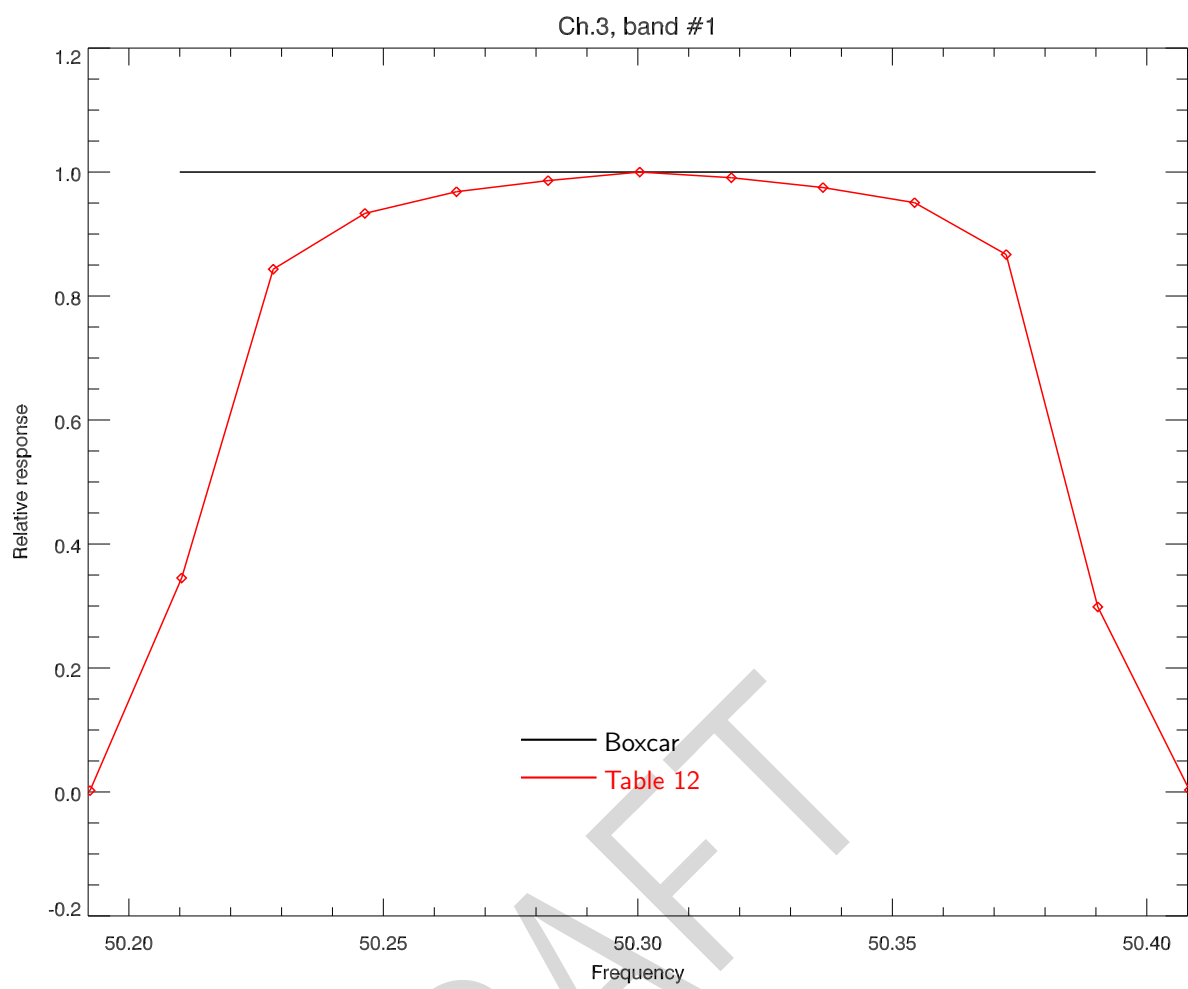


Figure A.3: NPP ATMS channel 3 response.

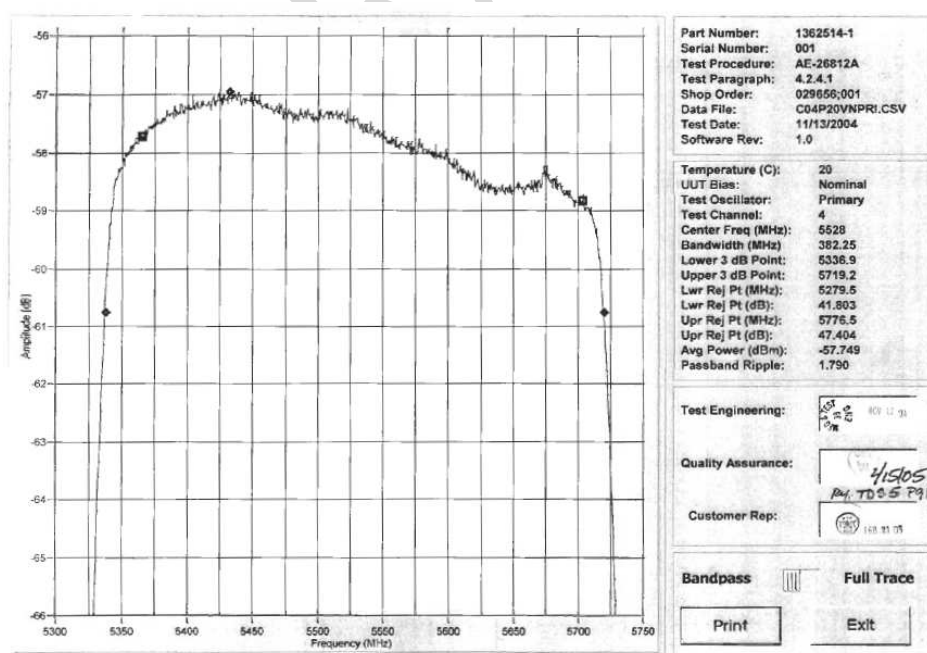
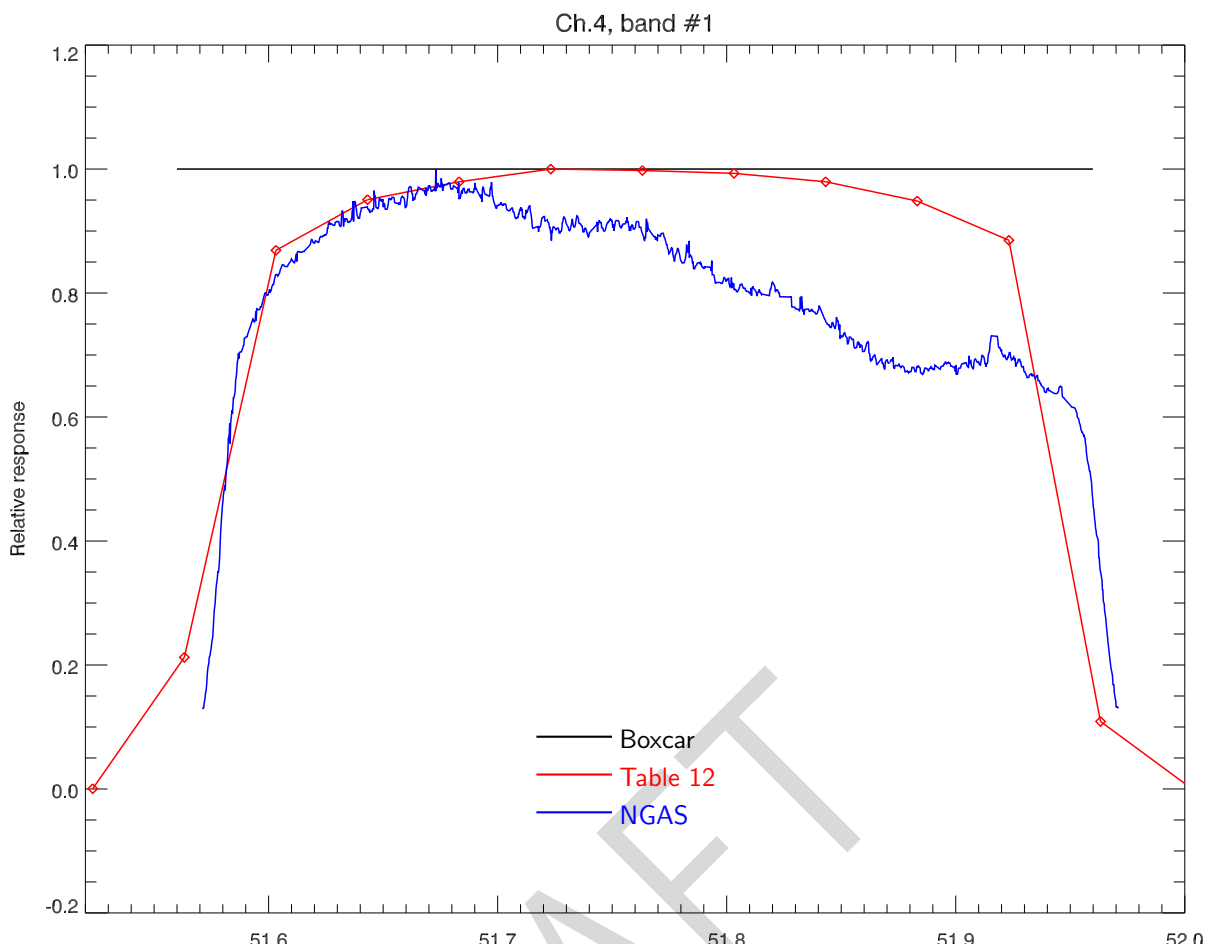


Figure A.4: NPP ATMS channel 4 response. **(Top)** Boxcar and digitised data. **(Bottom)** Nominal filter response from ATMS Calibration Data Book[1].

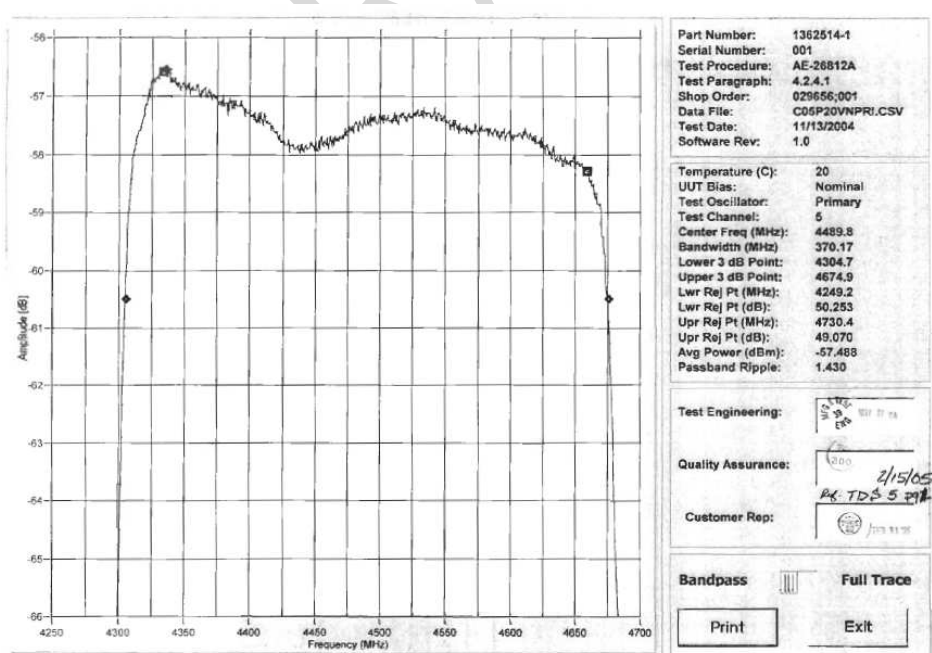
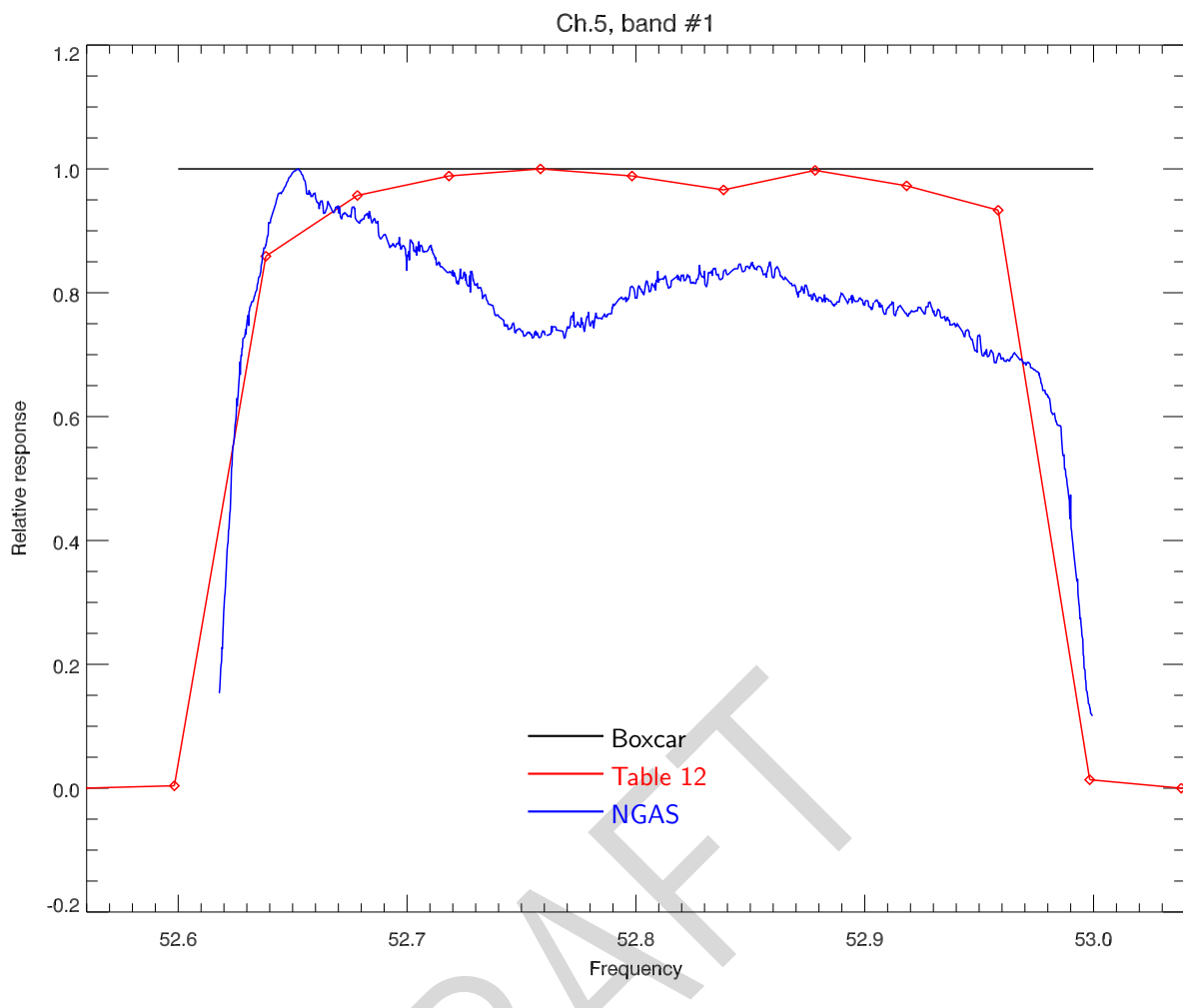


Figure A.5: NPP ATMS channel 5 response. **(Top)** Boxcar and digitised data. **(Bottom)** Nominal filter response from ATMS Calibration Data Book[1].

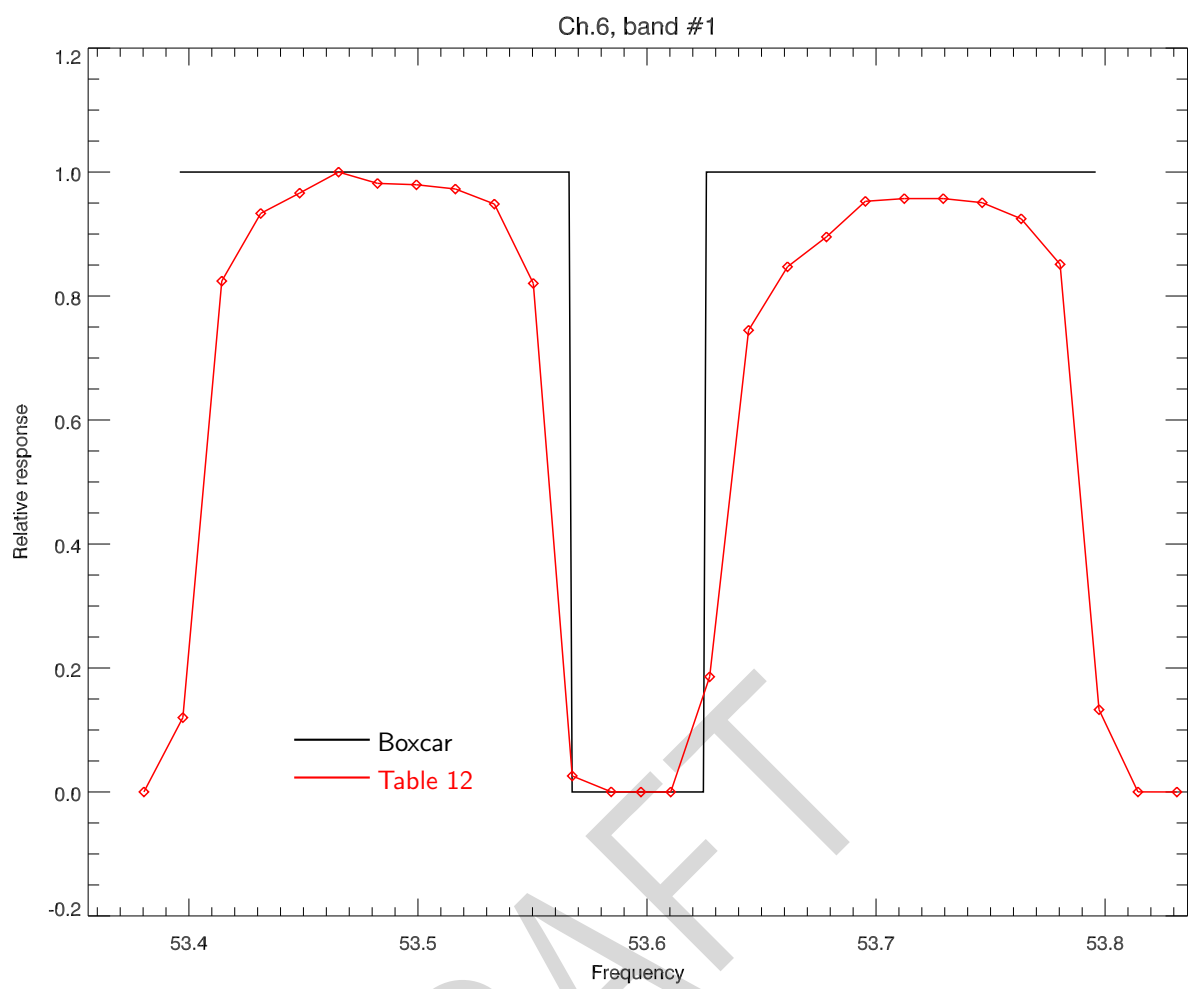


Figure A.6: NPP ATMS channel 6 response.

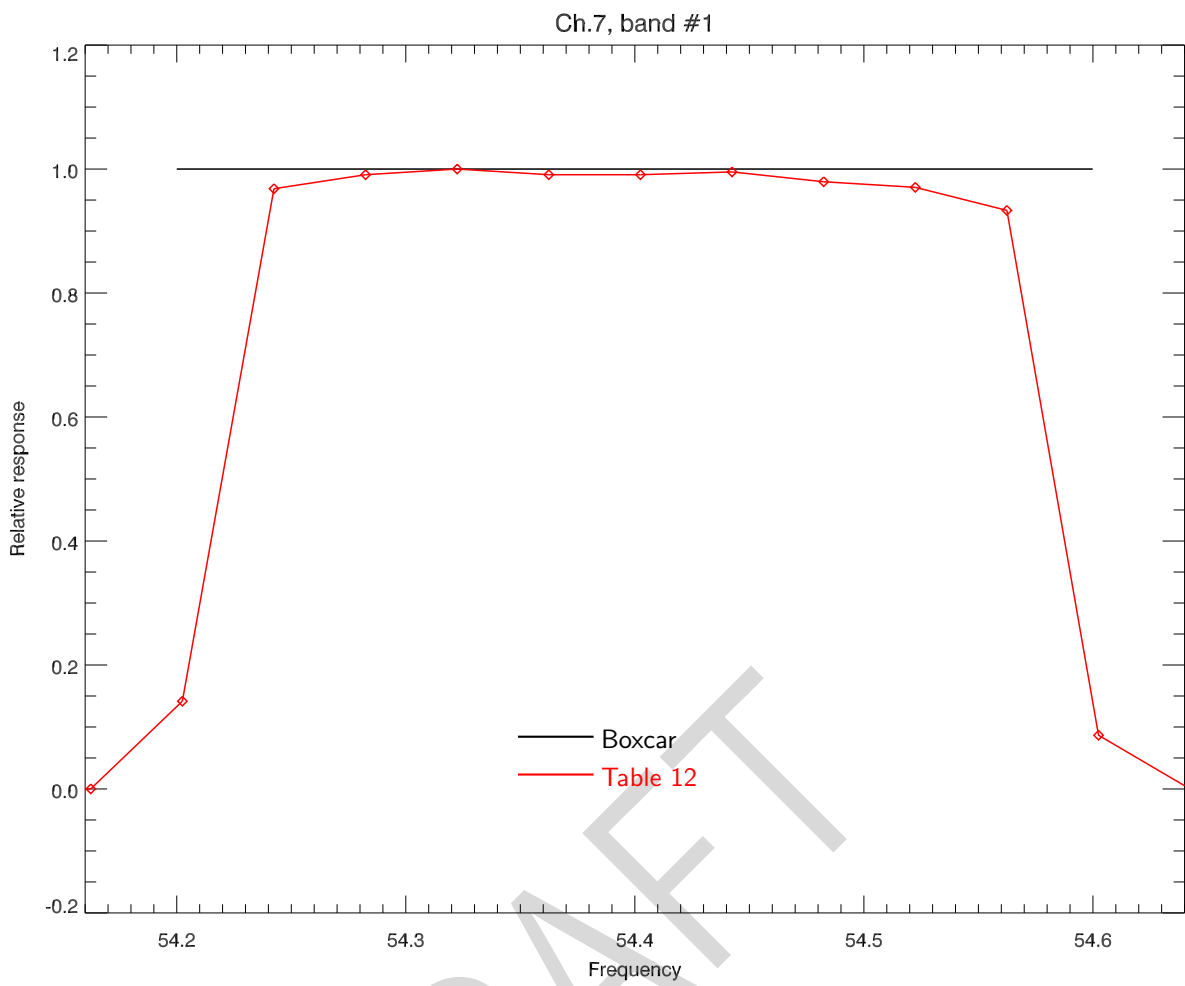


Figure A.7: NPP ATMS channel 7 response.

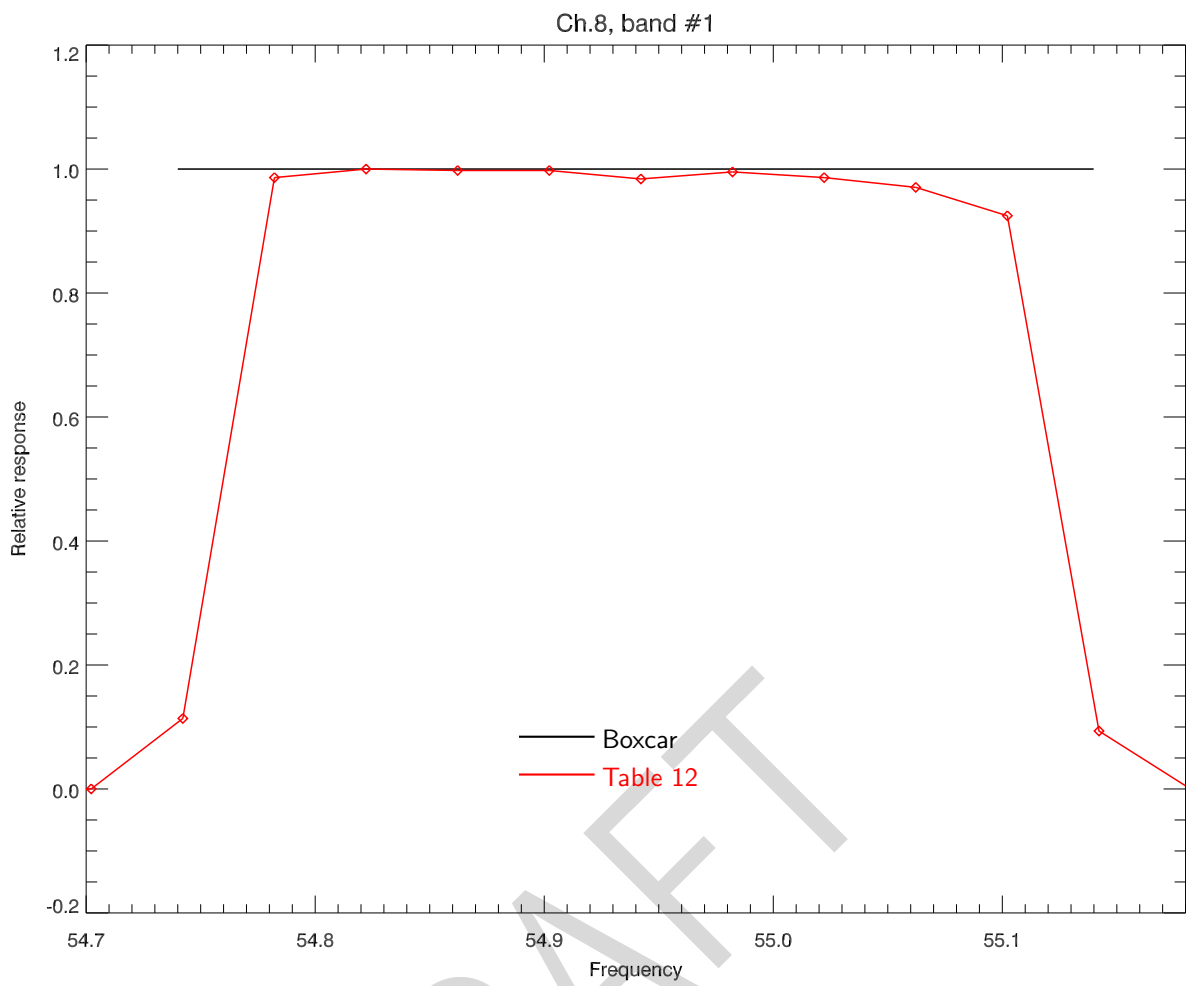


Figure A.8: NPP ATMS channel 8 response.

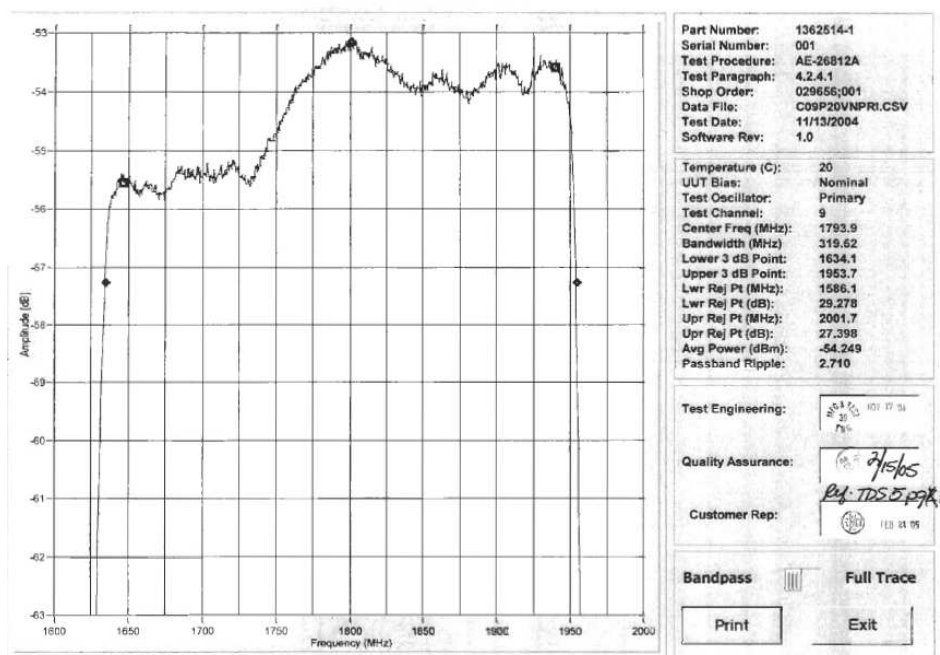
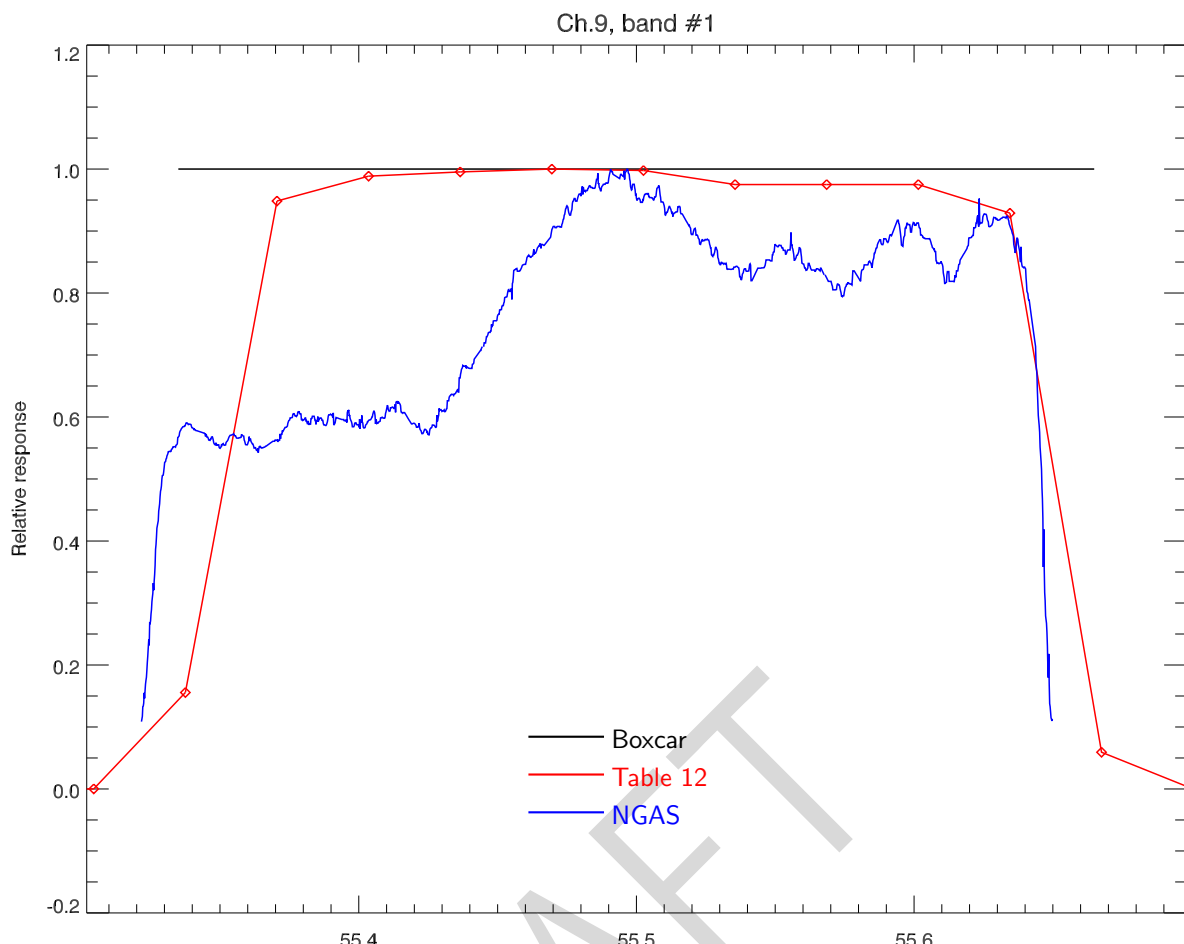


Figure A.9: NPP ATMS channel 9 response. **(Top)** Boxcar and digitised data. **(Bottom)** Nominal filter response from ATMS Calibration Data Book[1].

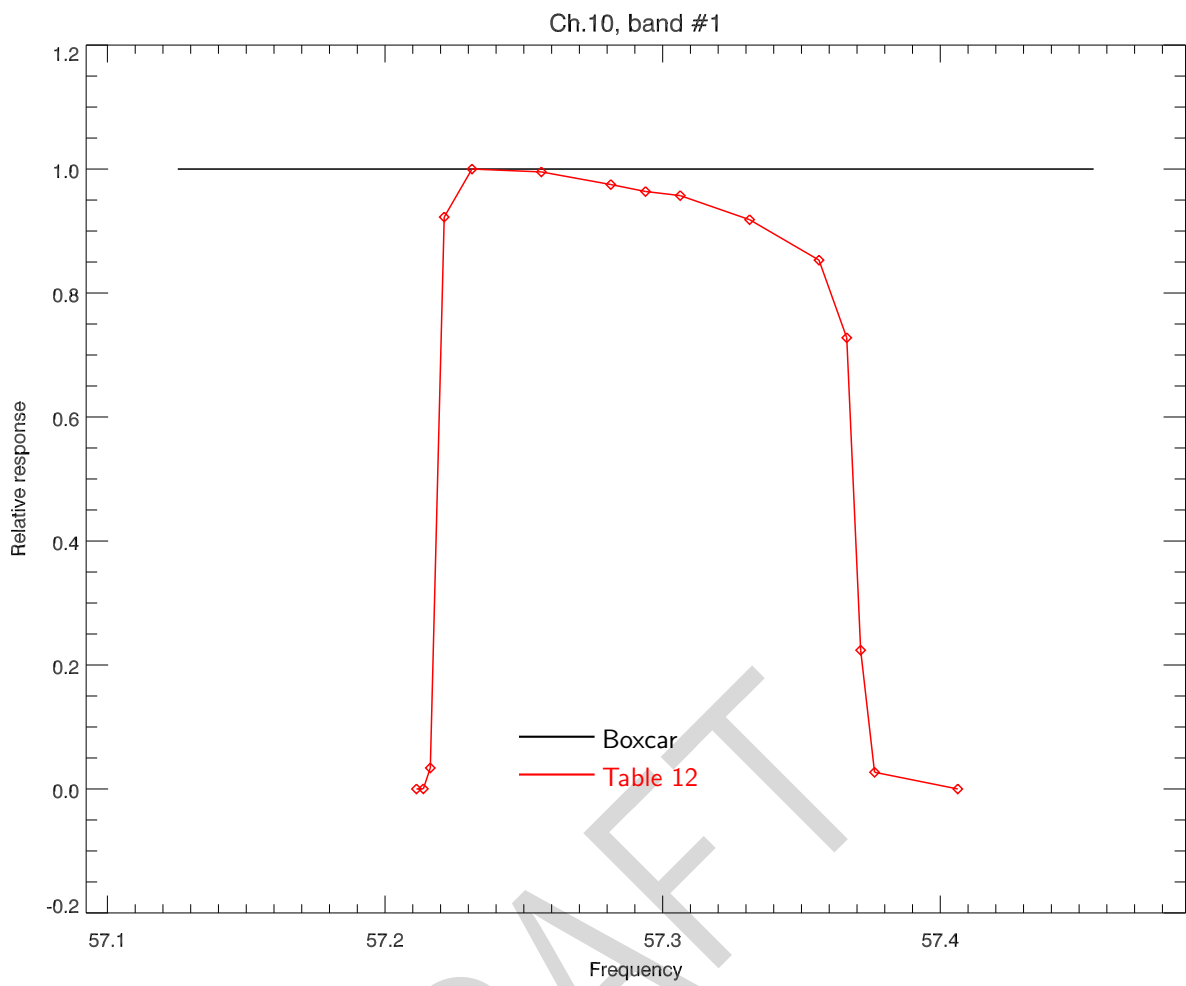


Figure A.10: NPP ATMS channel 10 response.

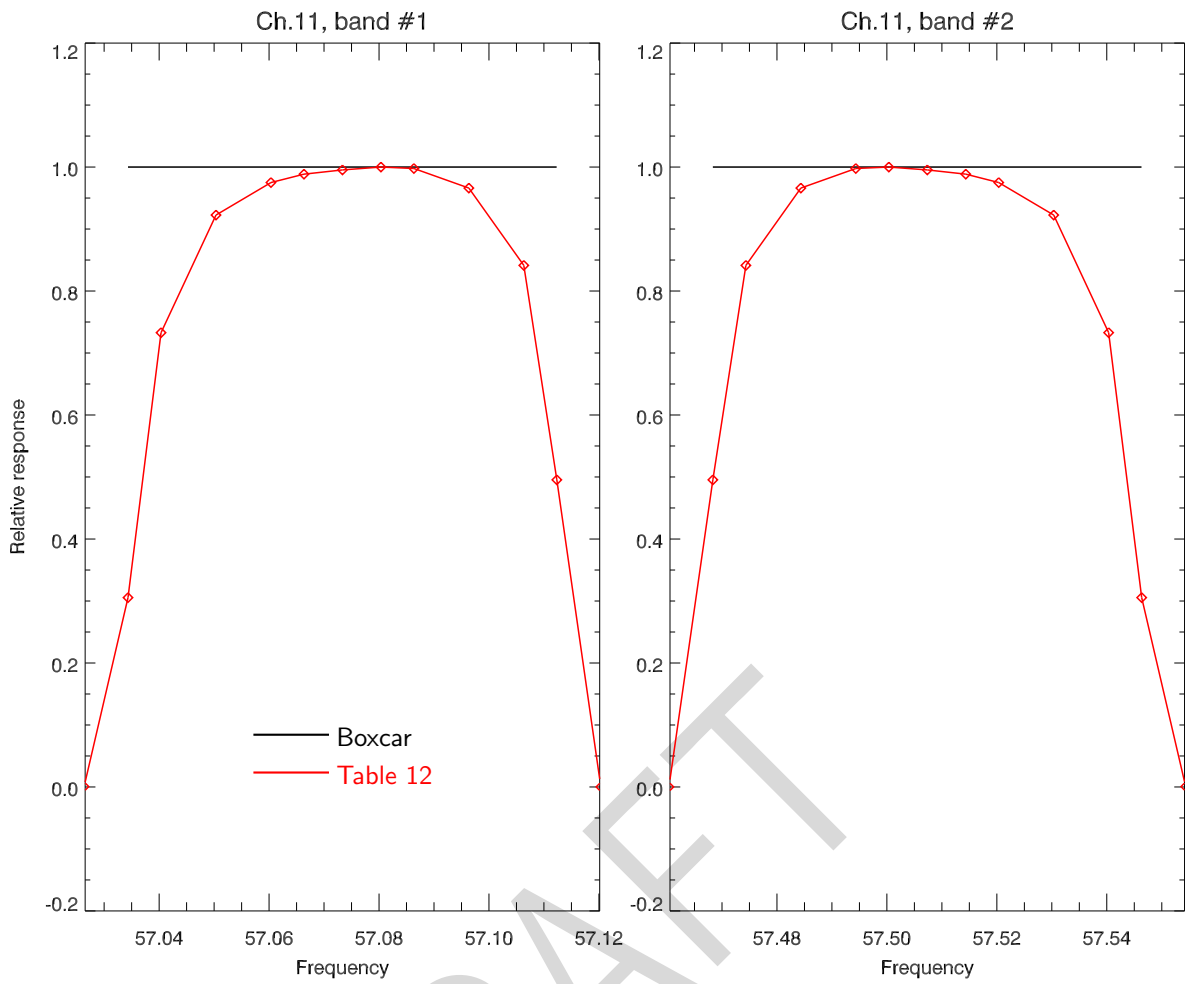


Figure A.11: NPP ATMS channel 11 response.

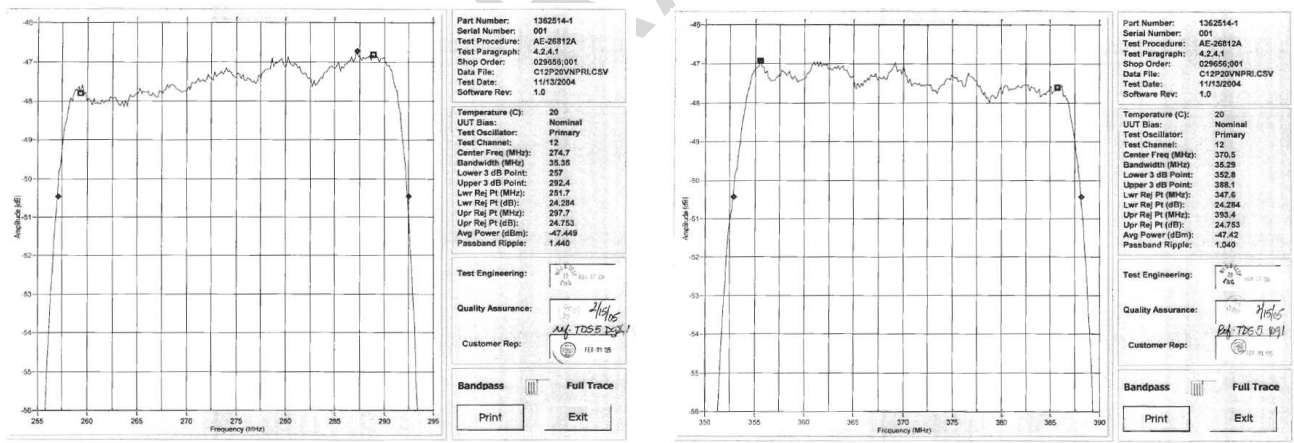
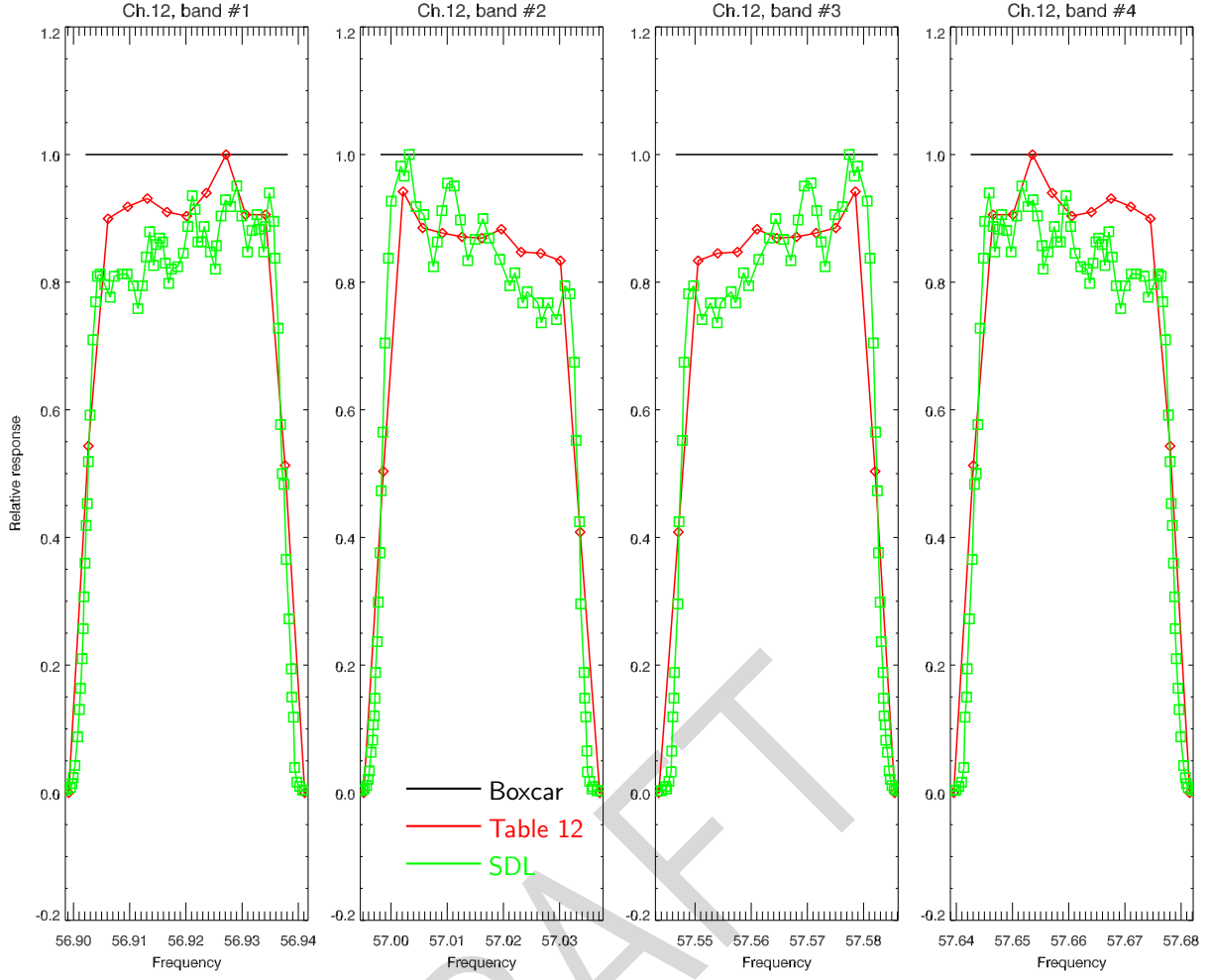


Figure A.12: NPP ATMS channel 12 response. **(Top)** Boxcar and digitised data. **(Bottom)** Nominal filter (low and high IF) response from ATMS Calibration Data Book[1]. The low IF (left) response corresponds to band #3 and the high IF (right) response to band #4.

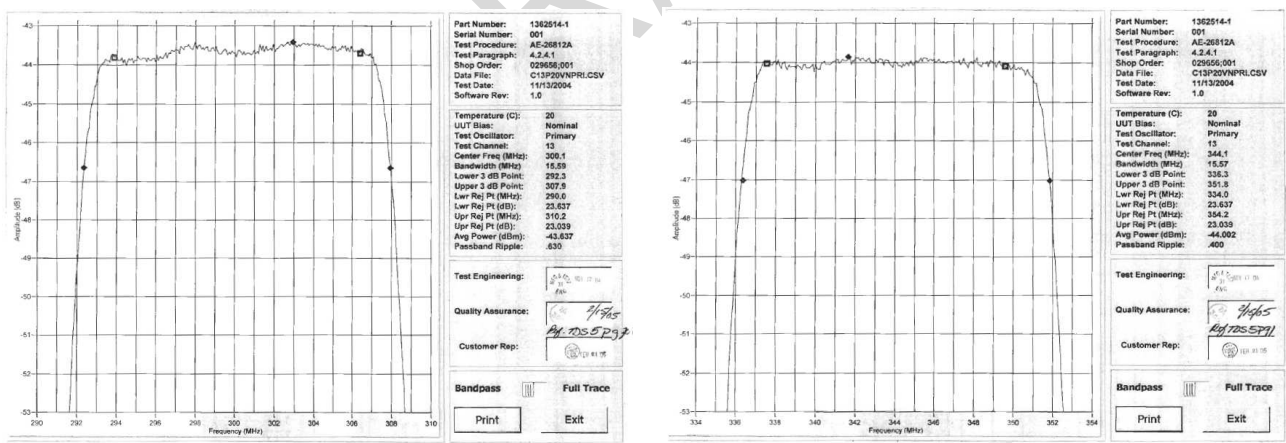
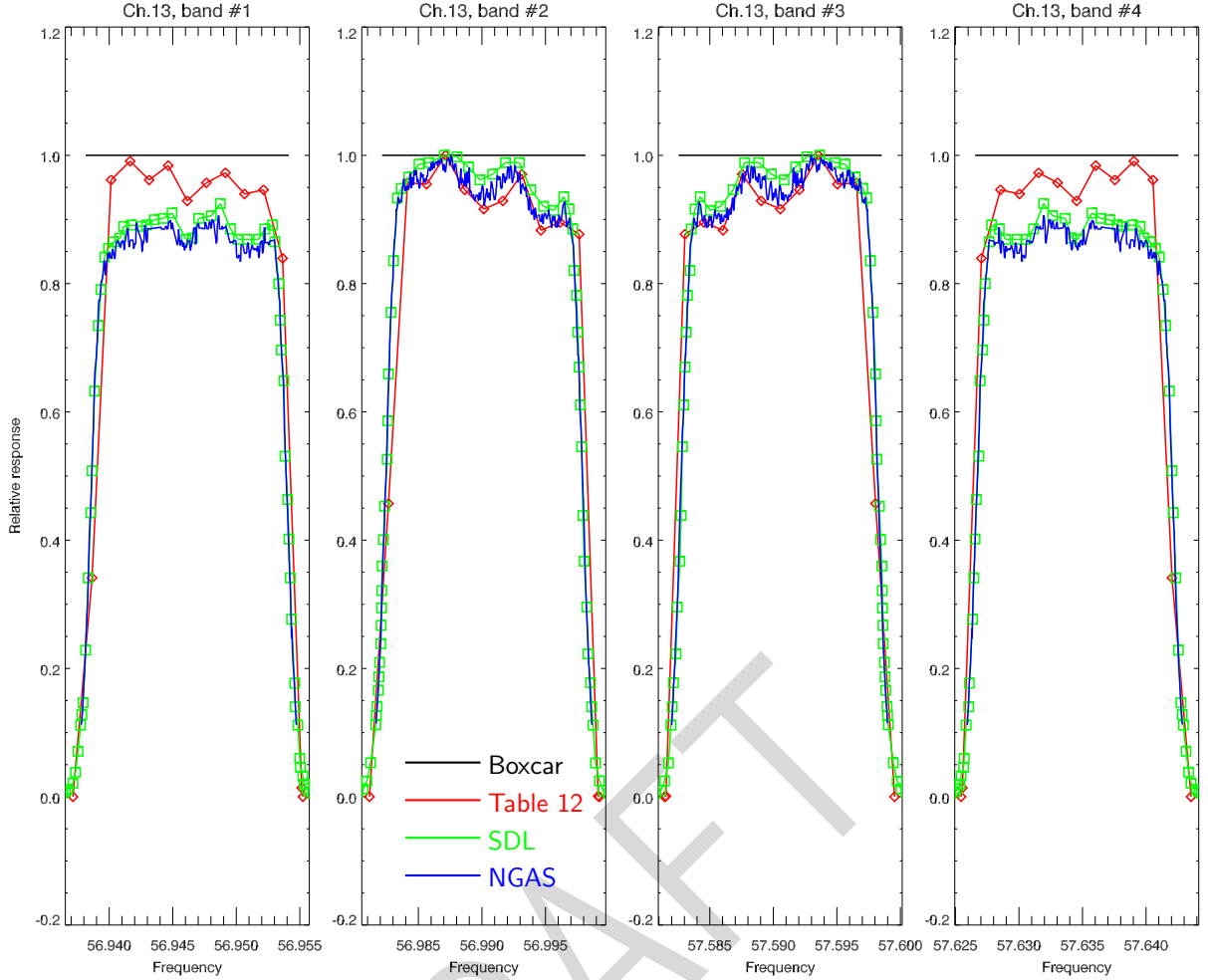


Figure A.13: NPP ATMS channel 13 response. **(Top)** Boxcar and digitised data. **(Bottom)** Nominal filter (low and high IF) response from ATMS Calibration Data Book[1]. The low IF (left) response corresponds to band #3 and the high IF (right) response to band #4.

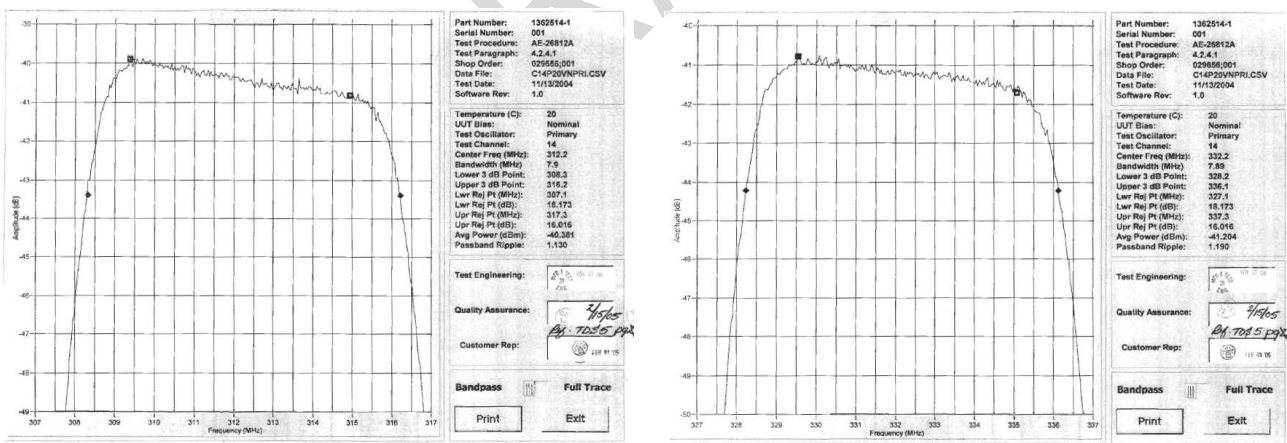
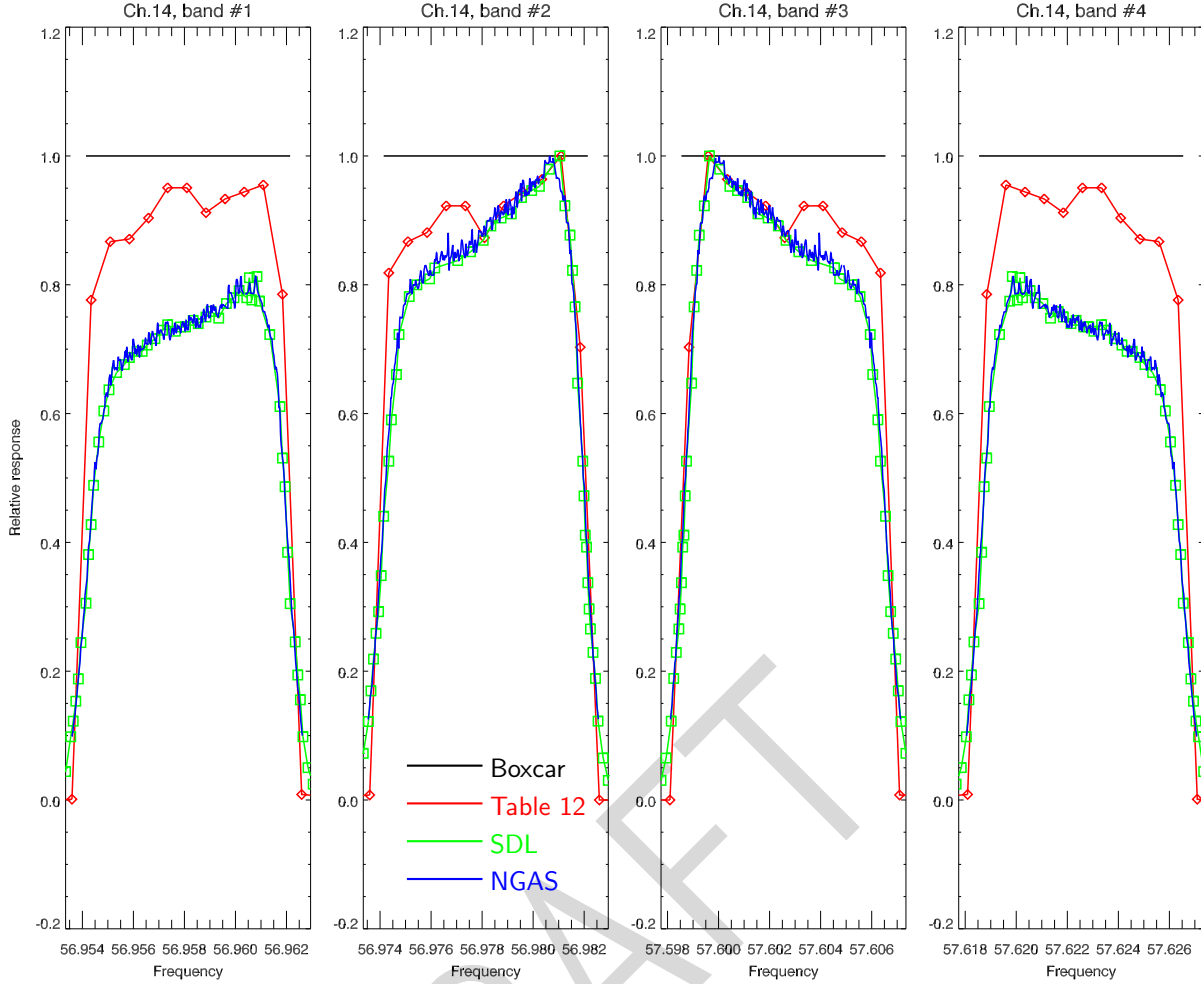


Figure A.14: NPP ATMS channel 14 response. **(Top)** Boxcar and digitised data. **(Bottom)** Nominal filter (low and high IF) response from ATMS Calibration Data Book[1]. The low IF (left) response corresponds to band #3 and the high IF (right) response to band #4.

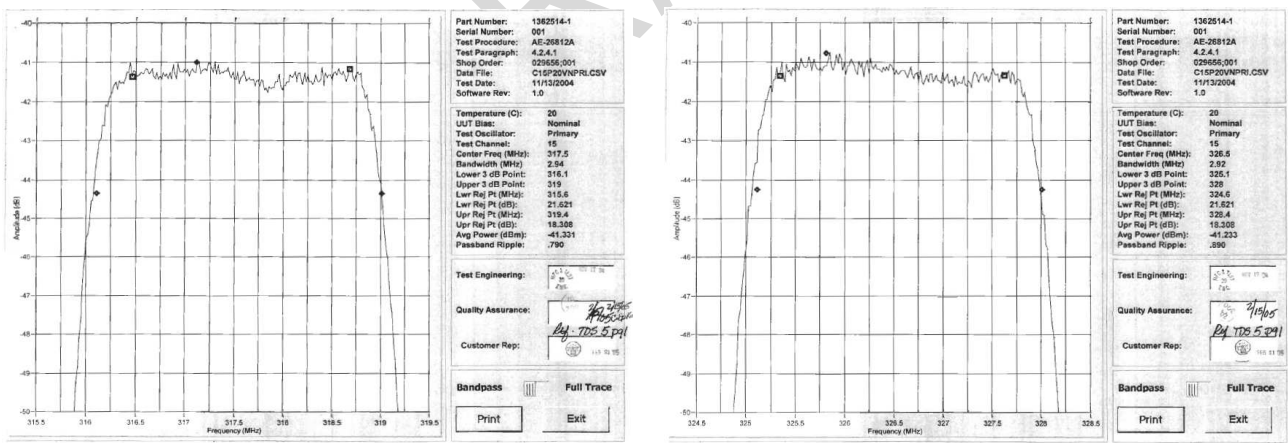
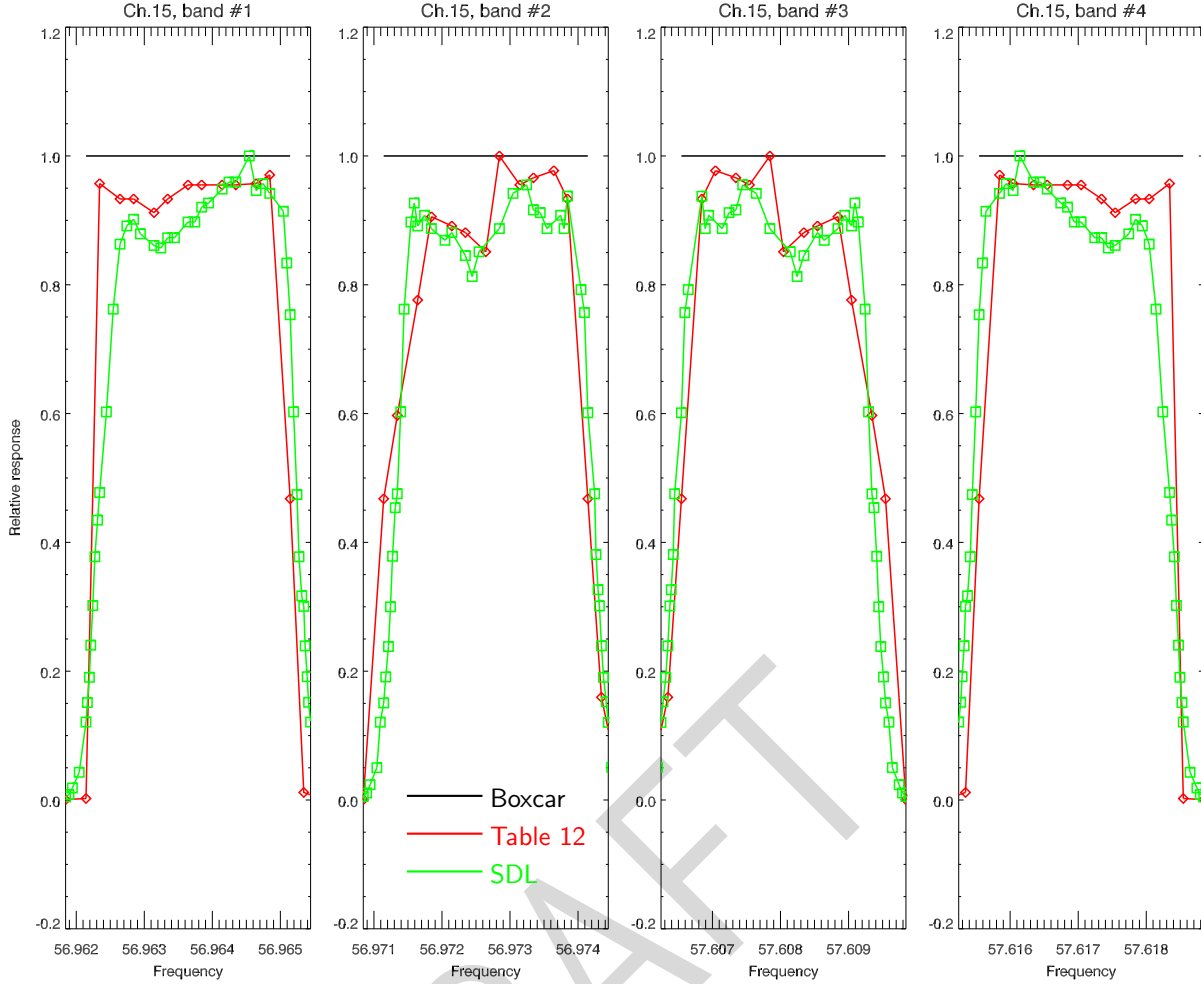


Figure A.15: NPP ATMS channel 15 response. **(Top)** Boxcar and digitised data. **(Bottom)** Nominal filter (low and high IF) response from ATMS Calibration Data Book[1]. The low IF (left) response corresponds to band #3 and the high IF (right) response to band #4.

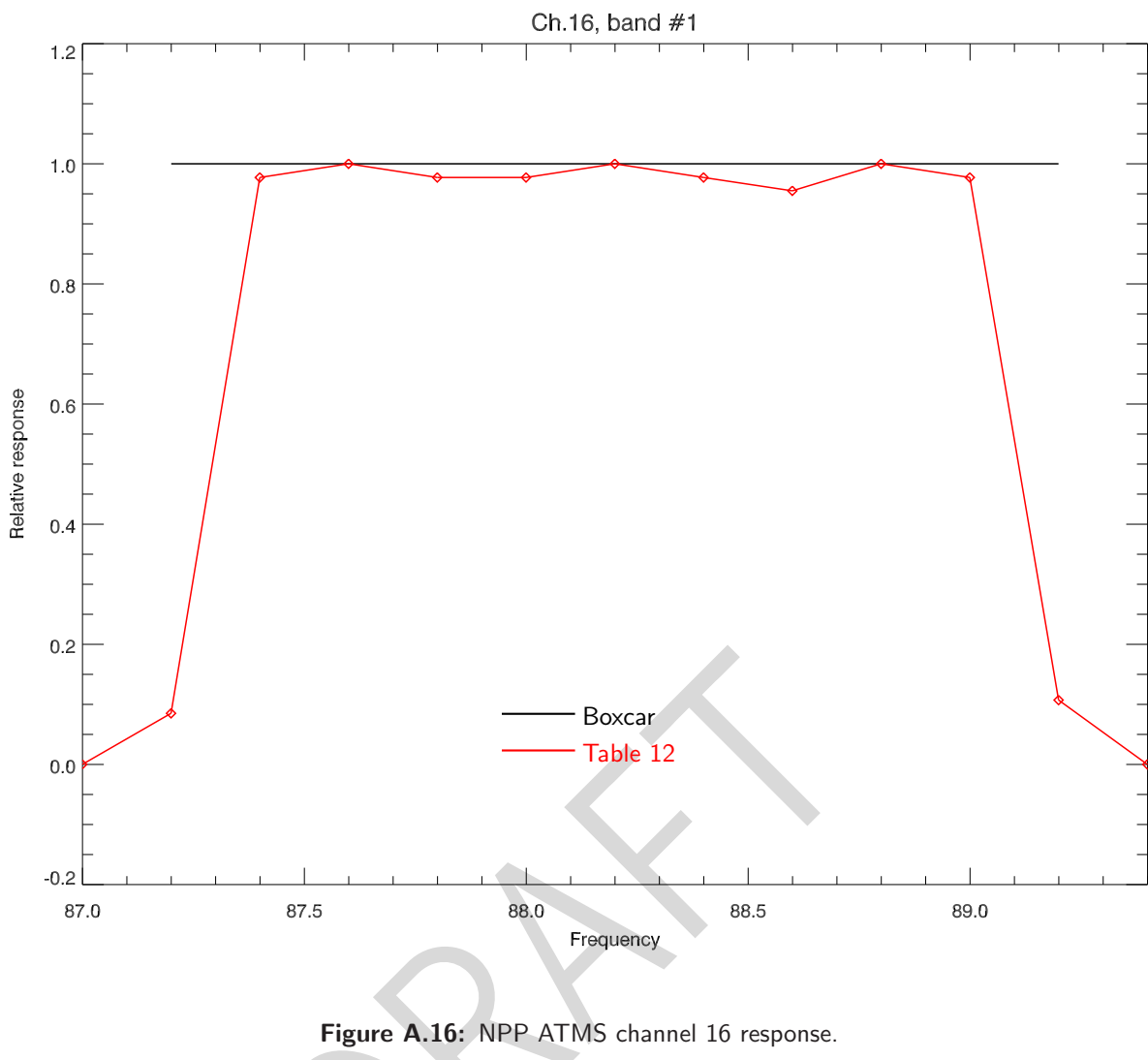


Figure A.16: NPP ATMS channel 16 response.

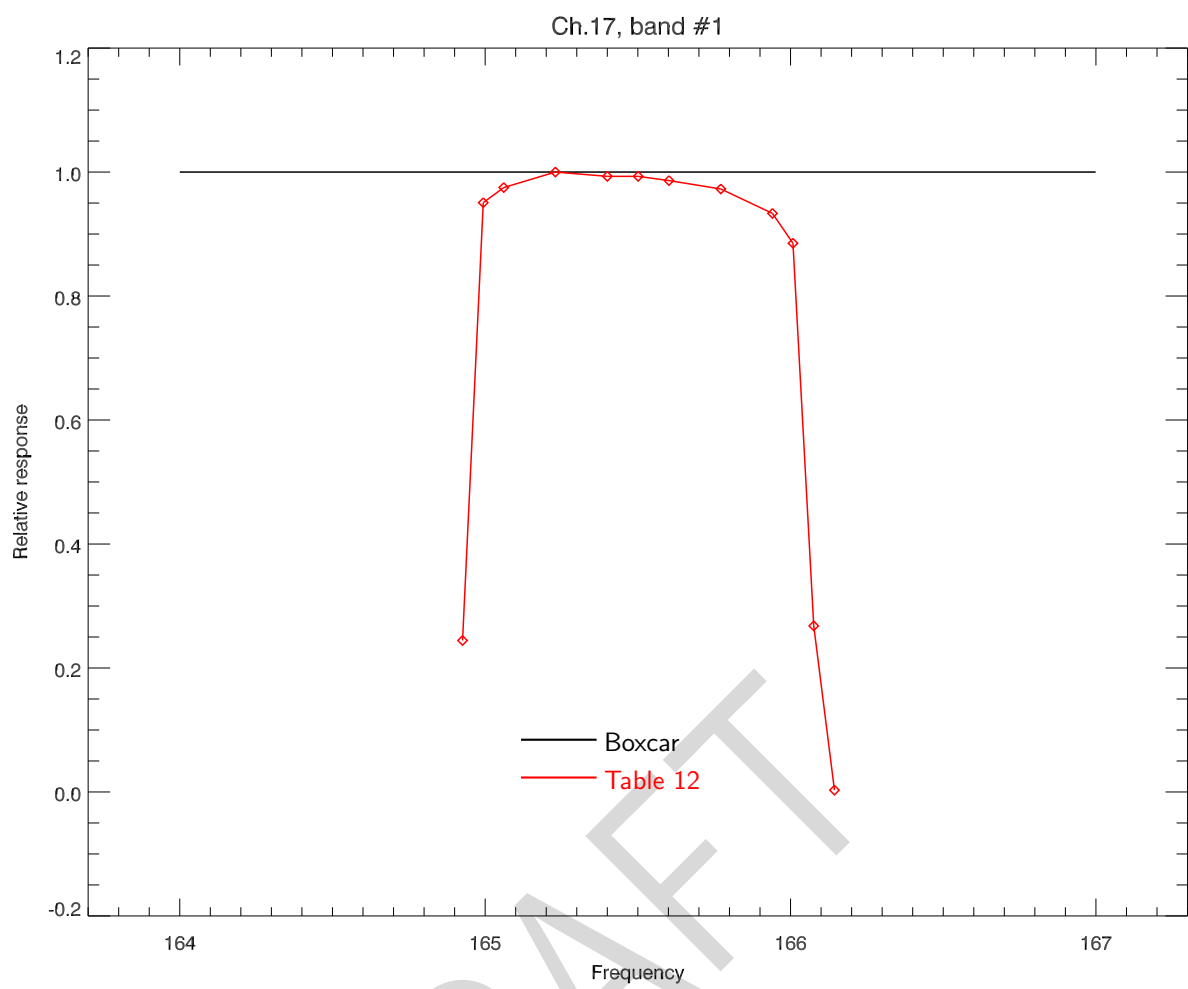


Figure A.17: NPP ATMS channel 17 response.

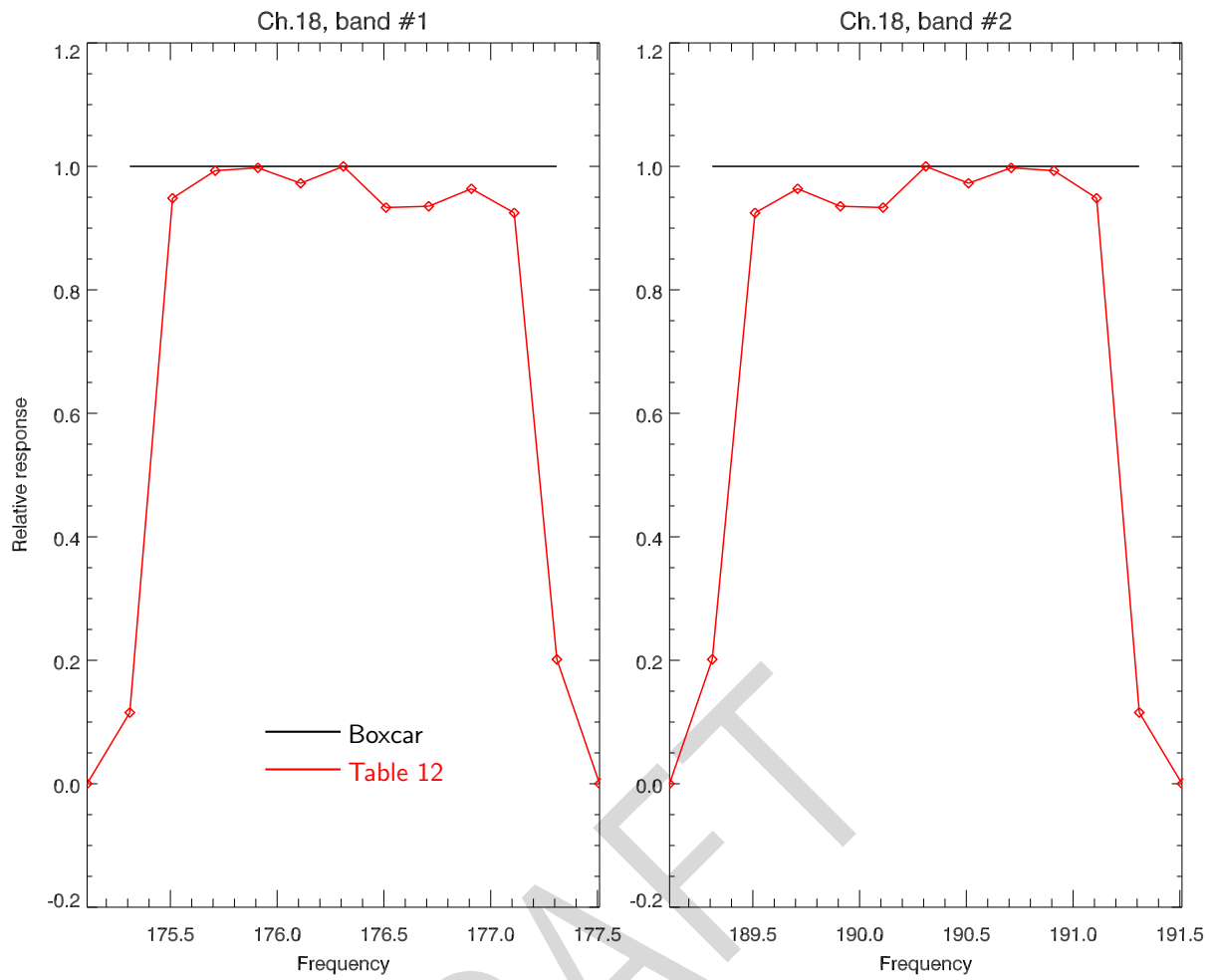


Figure A.18: NPP ATMS channel 18 response.

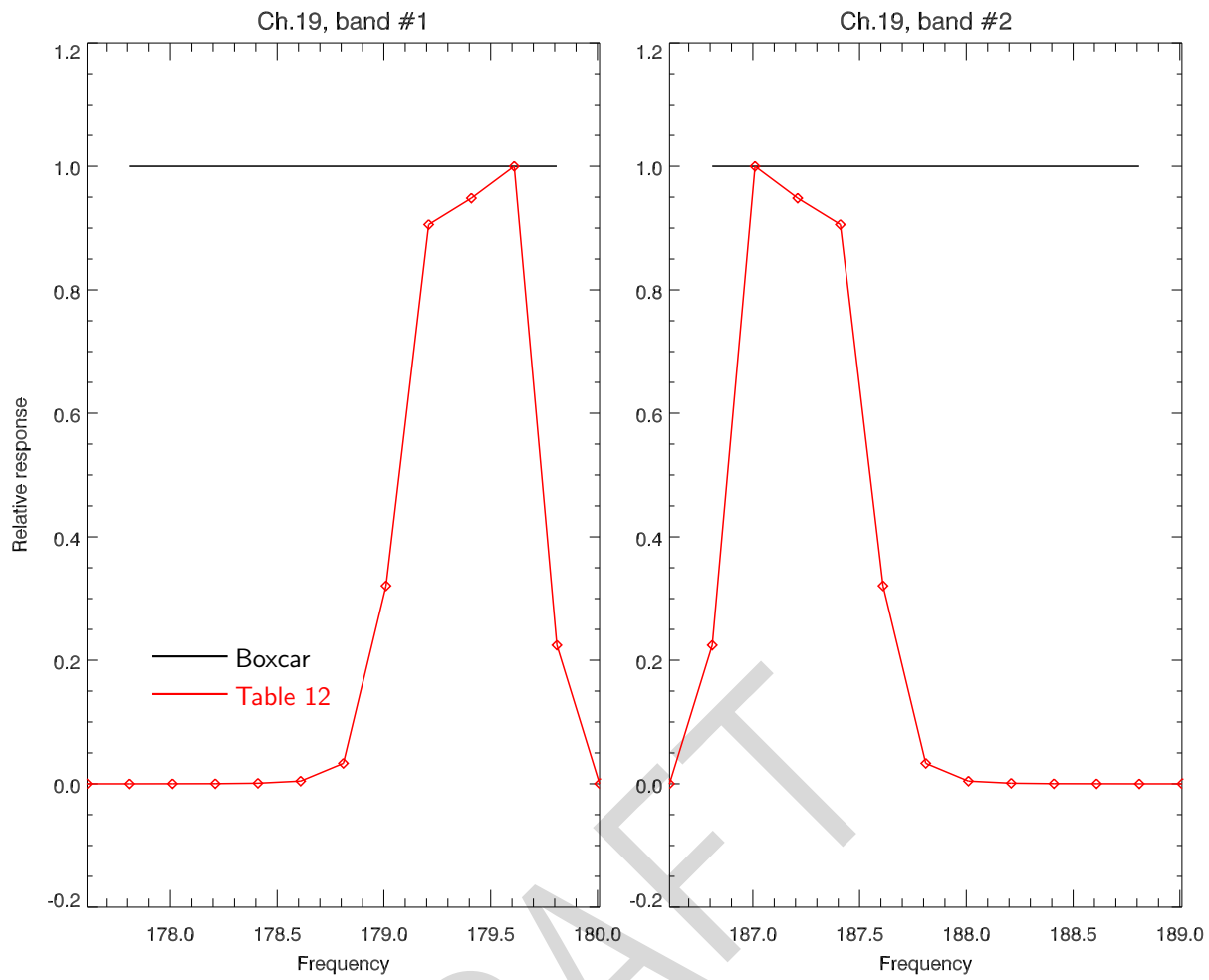


Figure A.19: NPP ATMS channel 19 response.

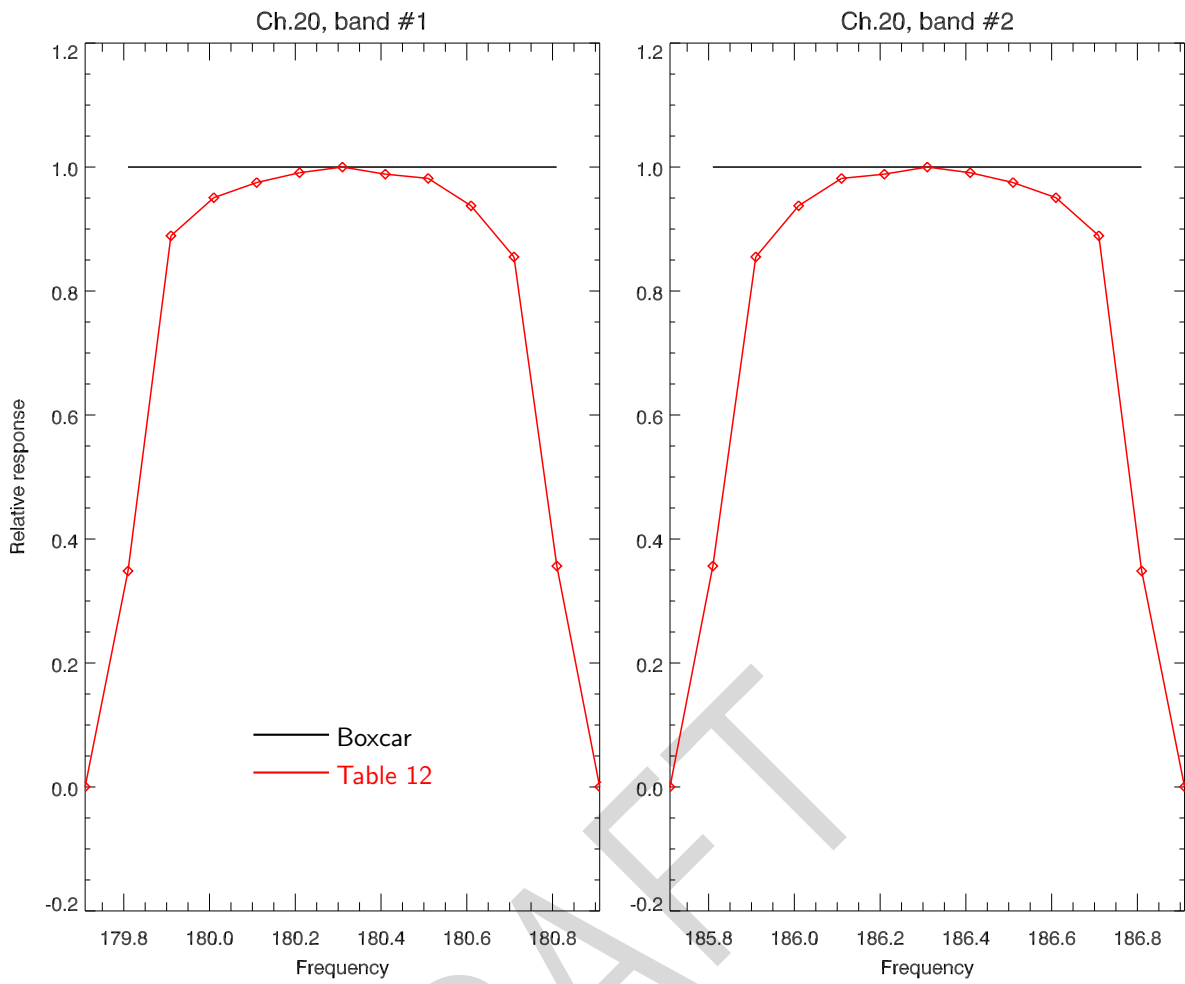


Figure A.20: NPP ATMS channel 20 response.

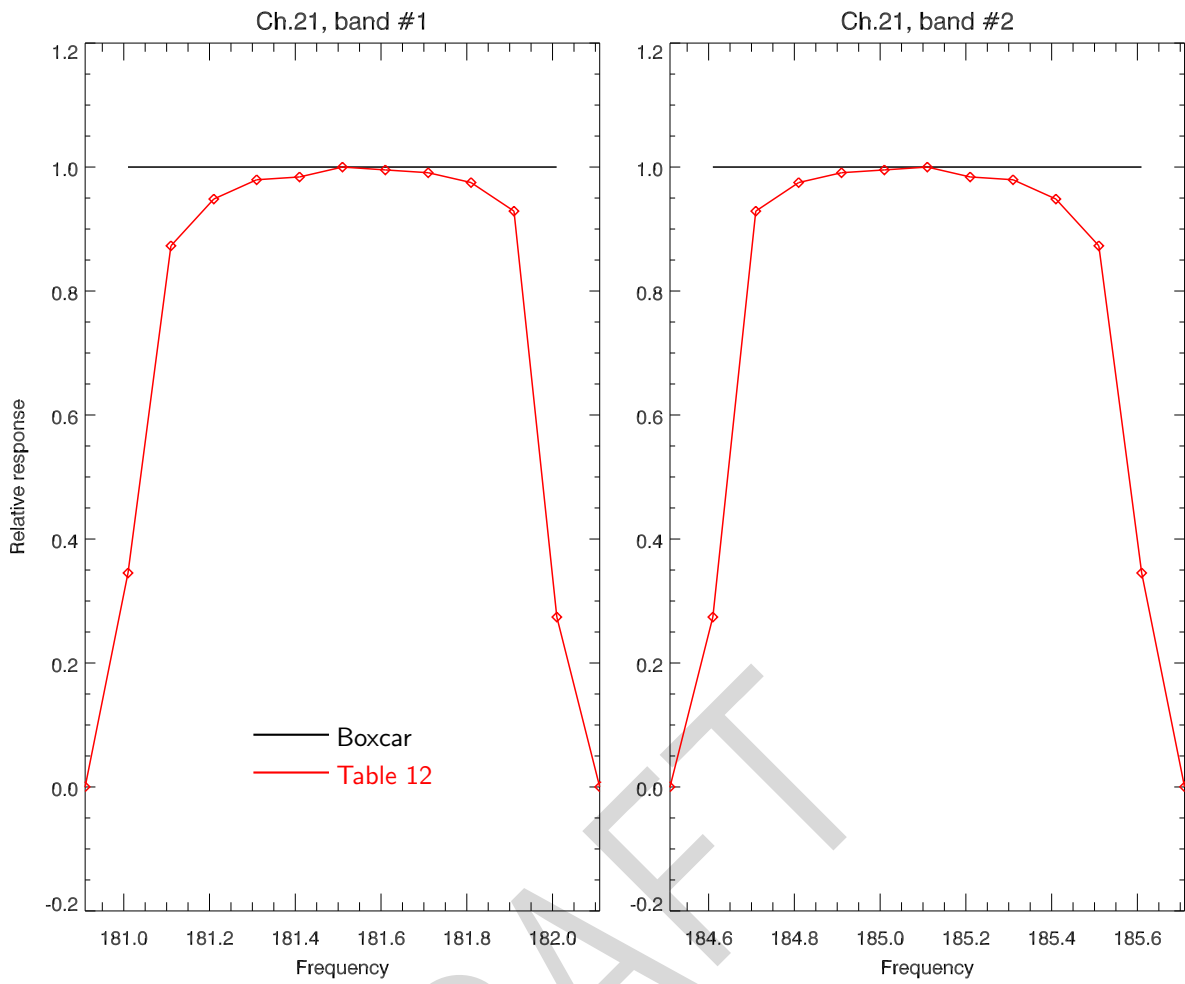


Figure A.21: NPP ATMS channel 21 response.

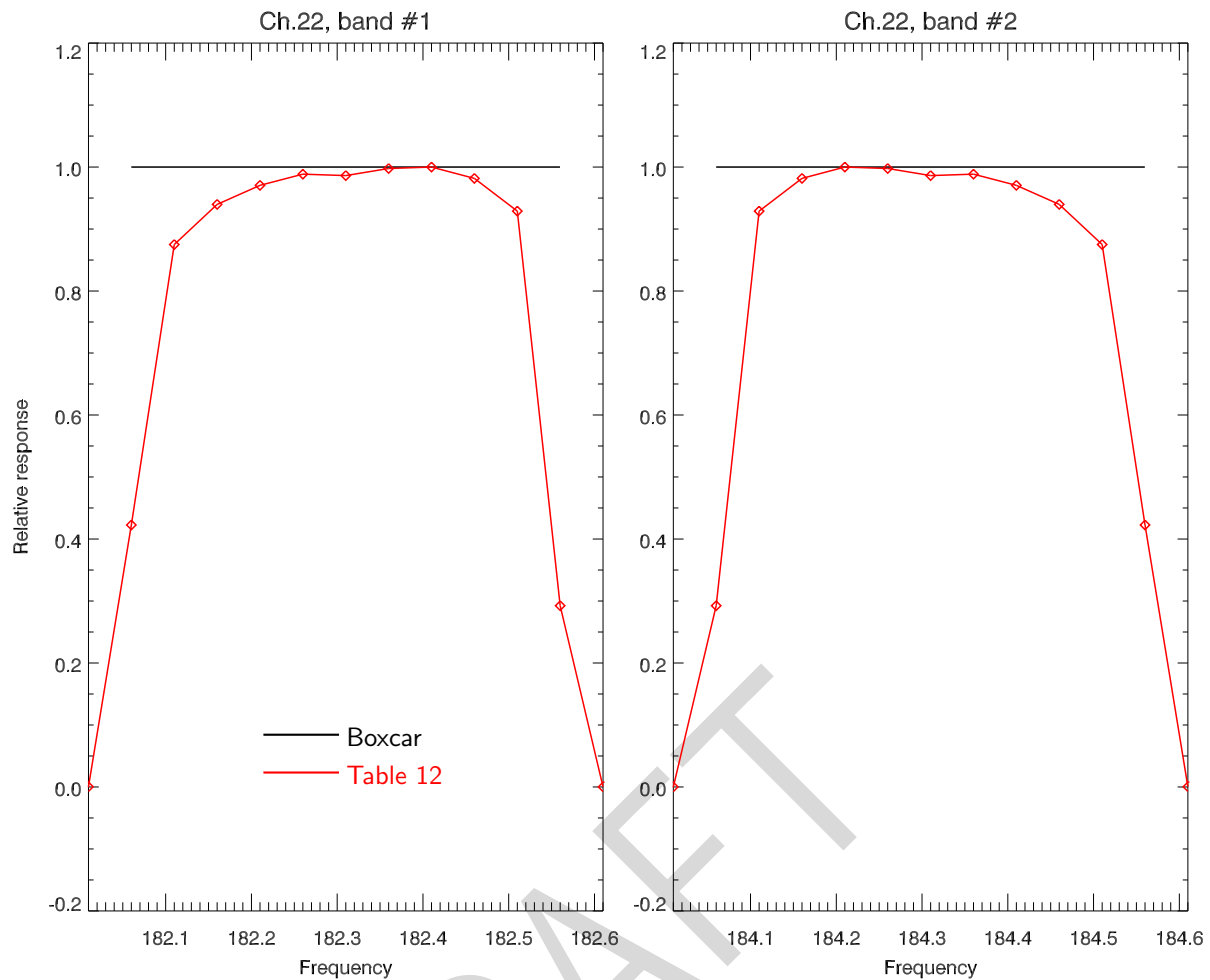


Figure A.22: NPP ATMS channel 22 response.

B ATMS NPP channel calculated brightness temperature comparisons

This section lists the calculated brightness temperature differences for the various measured SRFs with respect to the boxcar response. MonoRTM [5] was used to compute brightness temperatures for the ECMWF83 profile data set [3, 7] at the frequencies shown in the NPP ATMS SRF plots of appendix A. These monochromatic brightness temperatures were then integrated over frequency to provide the channel brightness temperatures.

DRAFT

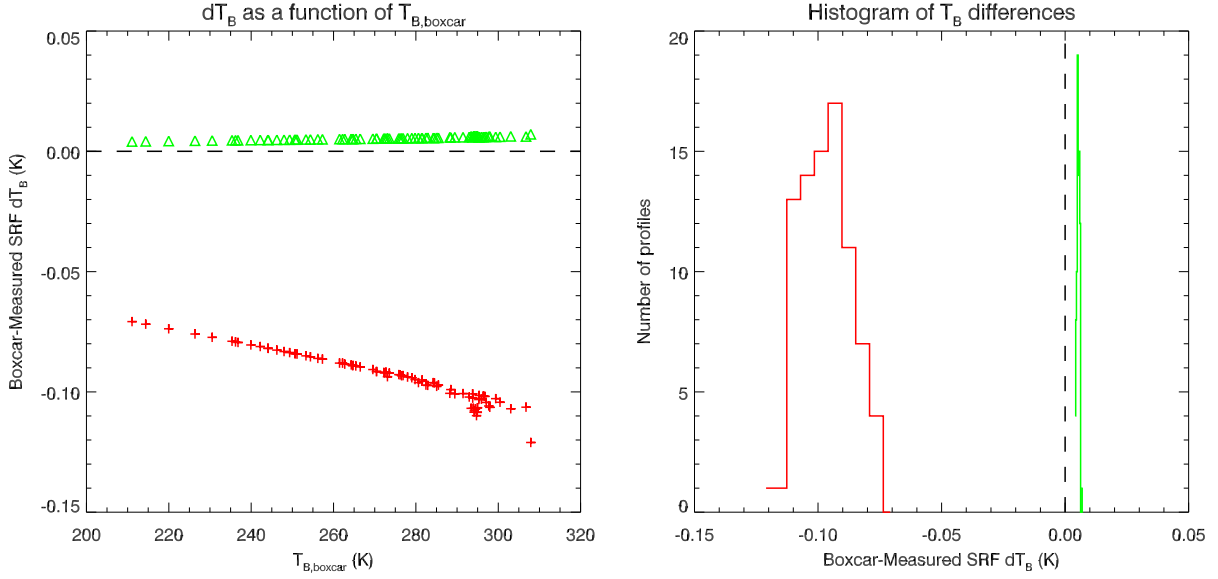


Figure B.1: NPP ATMS channel 1 calculated brightness temperature differences. **(Left)** ΔT_B as a function of the boxcar SRF T_B . **(Right)** Histogram of ΔT_B with respect to boxcar SRF T_B .

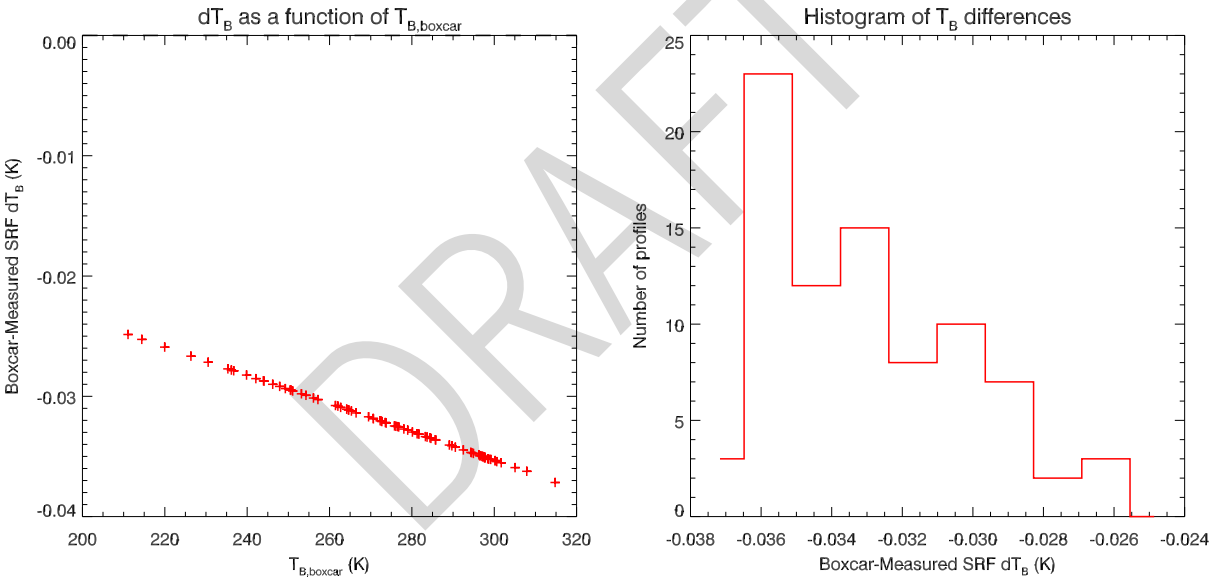


Figure B.2: NPP ATMS channel 2 calculated brightness temperature differences. **(Left)** ΔT_B as a function of the boxcar SRF T_B . **(Right)** Histogram of ΔT_B with respect to boxcar SRF T_B .

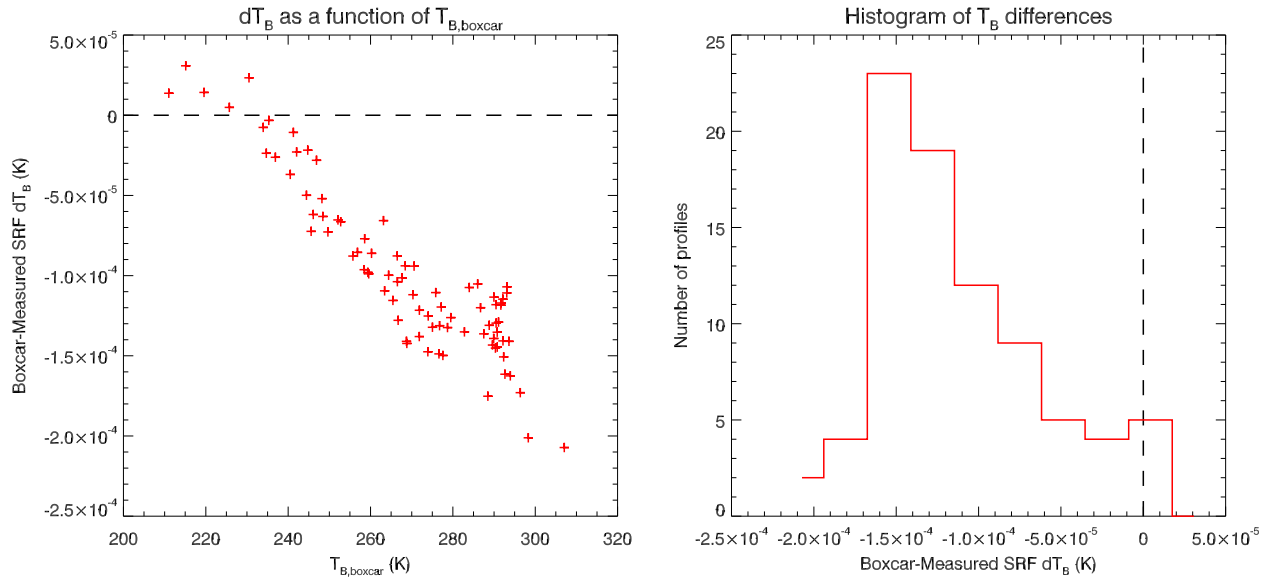


Figure B.3: NPP ATMS channel 3 calculated brightness temperature differences. **(Left)** ΔT_B as a function of the boxcar SRF T_B . **(Right)** Histogram of ΔT_B with respect to boxcar SRF T_B .

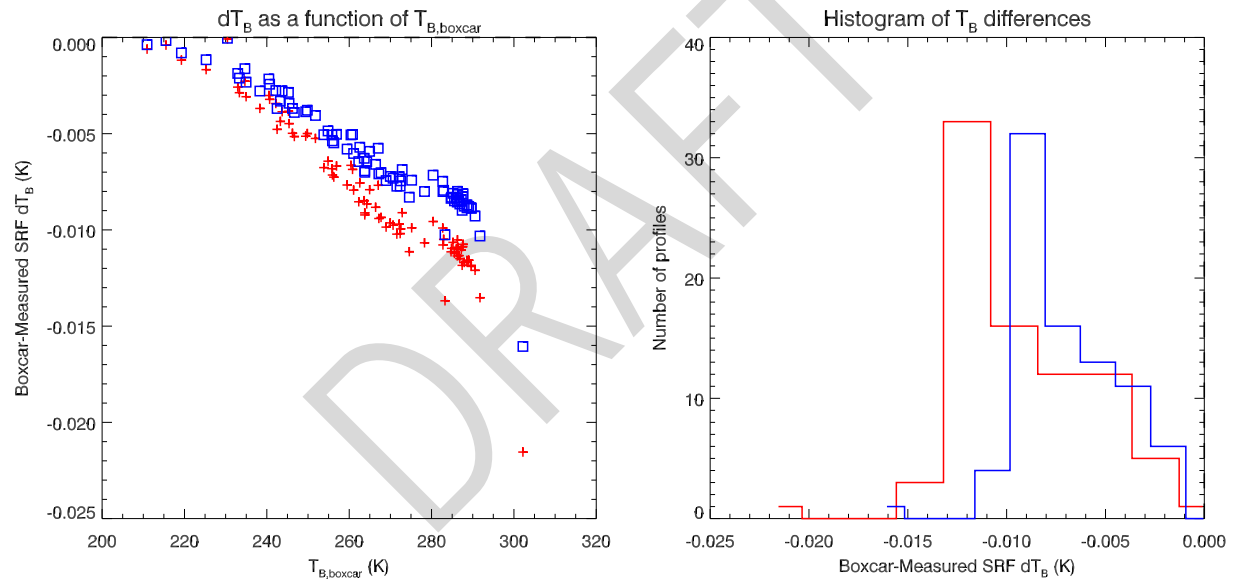


Figure B.4: NPP ATMS channel 4 calculated brightness temperature differences. **(Left)** ΔT_B as a function of the boxcar SRF T_B . **(Right)** Histogram of ΔT_B with respect to boxcar SRF T_B .

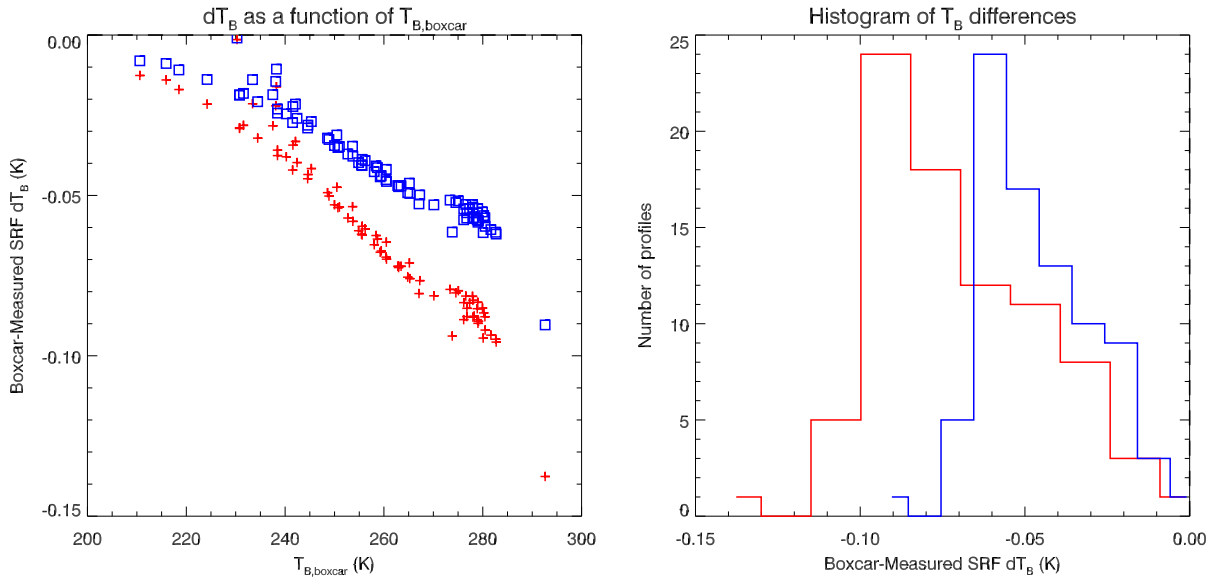


Figure B.5: NPP ATMS channel 5 calculated brightness temperature differences. **(Left)** ΔT_B as a function of the boxcar SRF T_B . **(Right)** Histogram of ΔT_B with respect to boxcar SRF T_B .

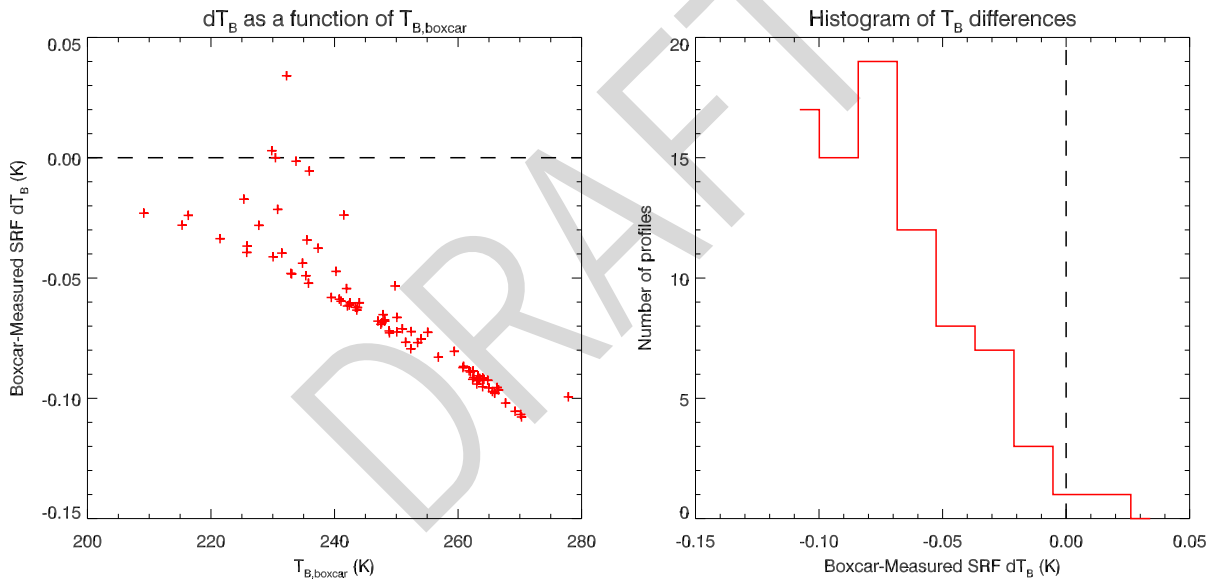


Figure B.6: NPP ATMS channel 6 calculated brightness temperature differences. **(Left)** ΔT_B as a function of the boxcar SRF T_B . **(Right)** Histogram of ΔT_B with respect to boxcar SRF T_B .

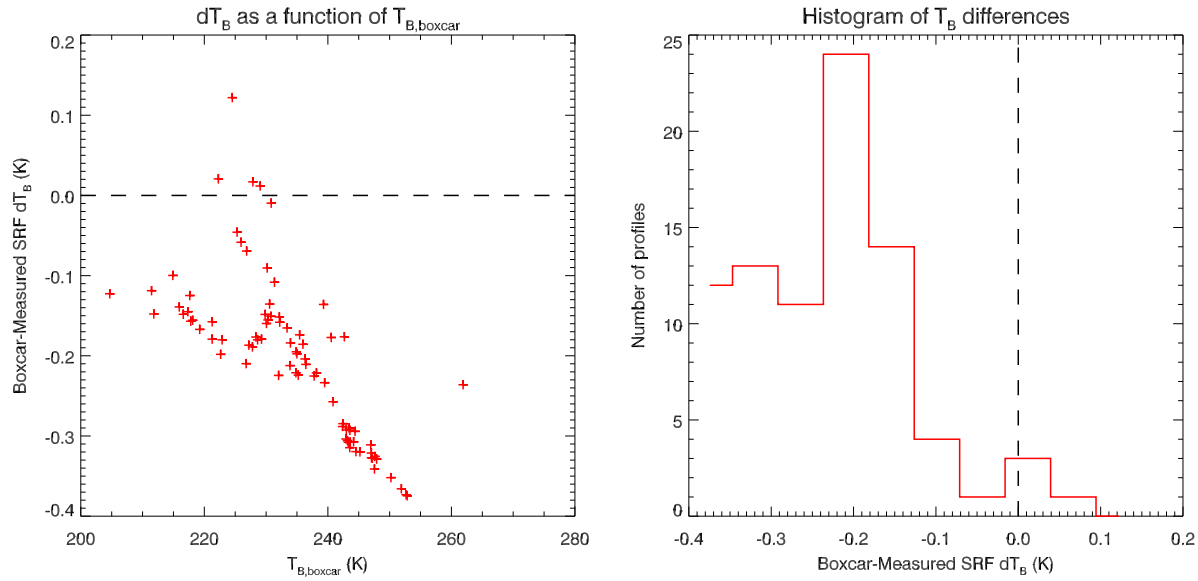


Figure B.7: NPP ATMS channel 7 calculated brightness temperature differences. **(Left)** ΔT_B as a function of the boxcar SRF T_B . **(Right)** Histogram of ΔT_B with respect to boxcar SRF T_B .

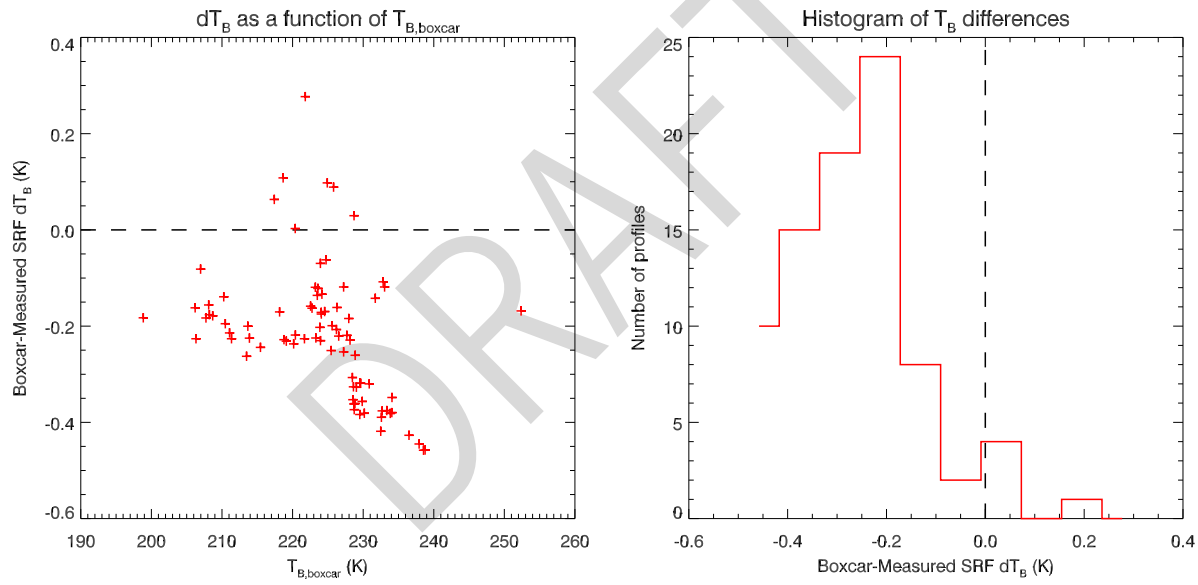


Figure B.8: NPP ATMS channel 8 calculated brightness temperature differences. **(Left)** ΔT_B as a function of the boxcar SRF T_B . **(Right)** Histogram of ΔT_B with respect to boxcar SRF T_B .

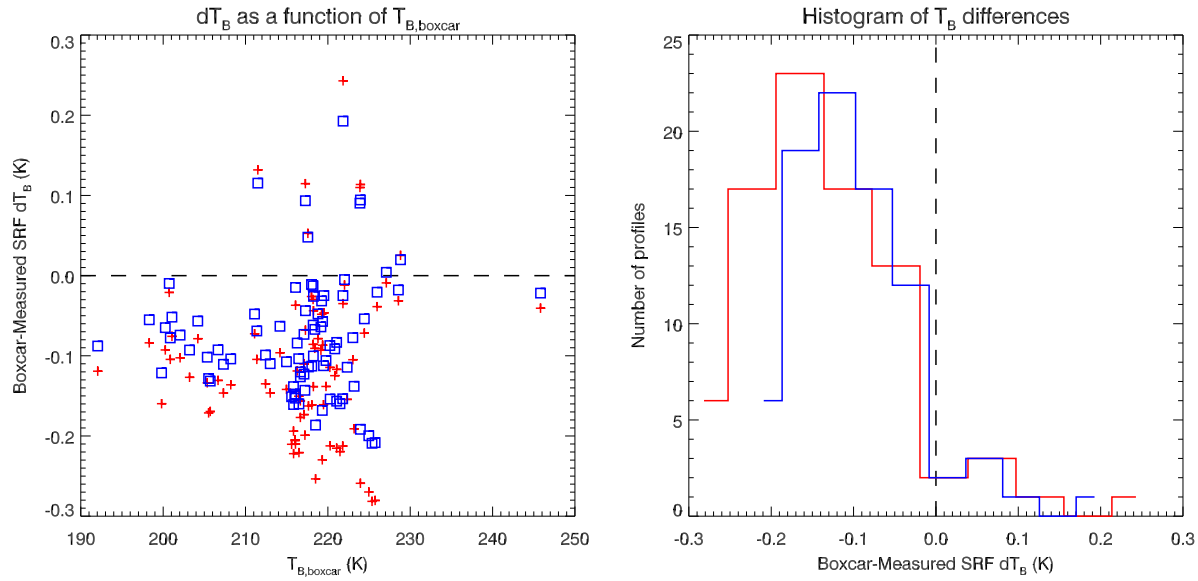


Figure B.9: NPP ATMS channel 9 calculated brightness temperature differences. **(Left)** ΔT_B as a function of the boxcar SRF T_B . **(Right)** Histogram of ΔT_B with respect to boxcar SRF T_B .

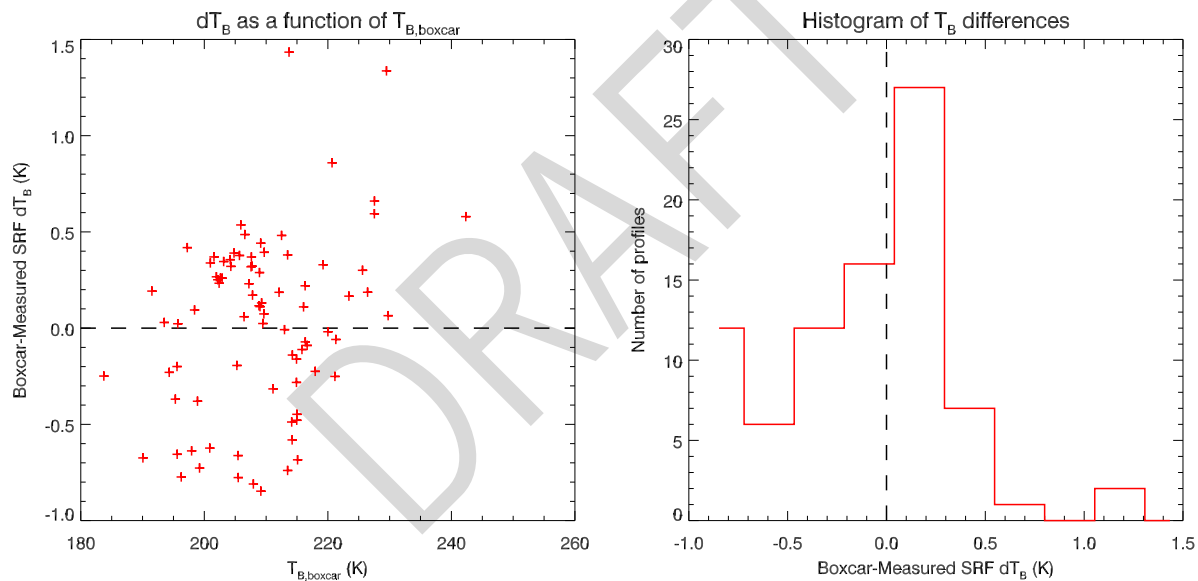


Figure B.10: NPP ATMS channel 10 calculated brightness temperature differences. **(Left)** ΔT_B as a function of the boxcar SRF T_B . **(Right)** Histogram of ΔT_B with respect to boxcar SRF T_B .

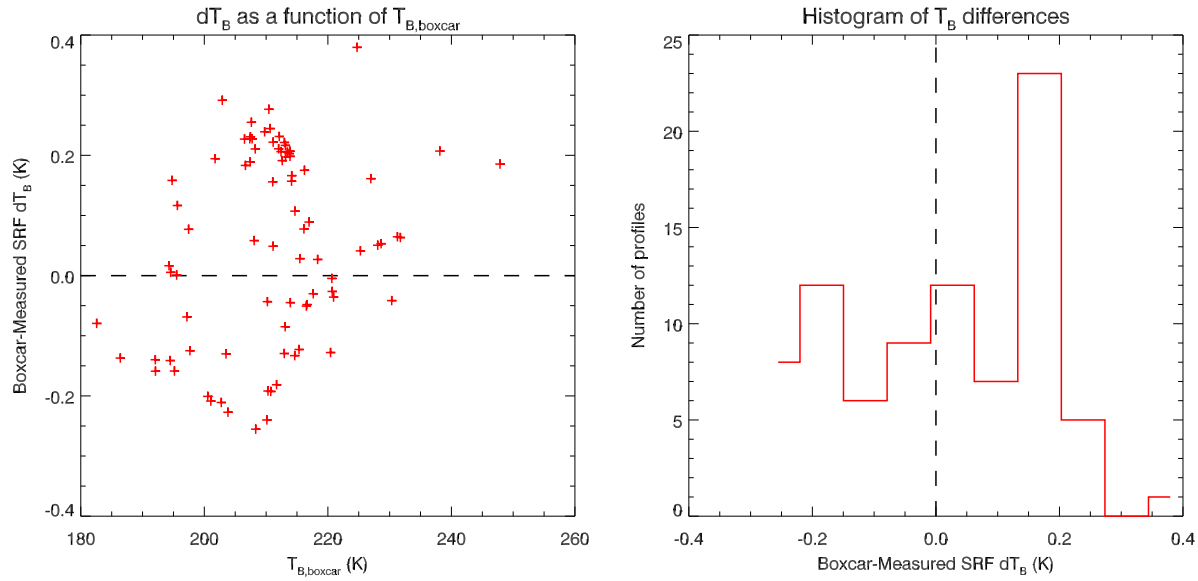


Figure B.11: NPP ATMS channel 11 calculated brightness temperature differences. **(Left)** ΔT_B as a function of the boxcar SRF T_B . **(Right)** Histogram of ΔT_B with respect to boxcar SRF T_B .

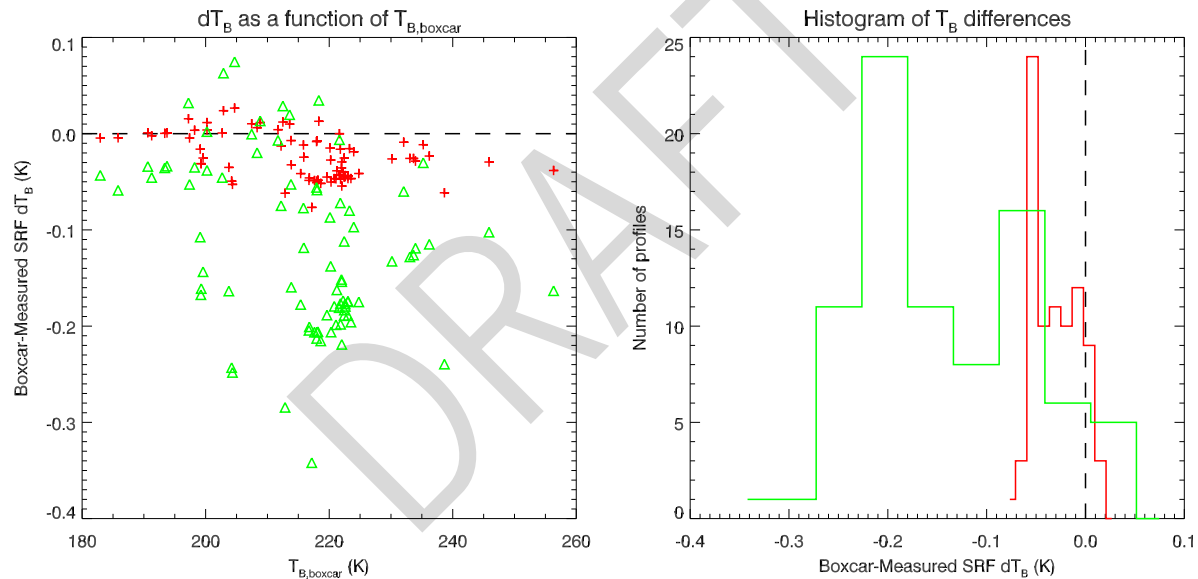


Figure B.12: NPP ATMS channel 12 calculated brightness temperature differences. **(Left)** ΔT_B as a function of the boxcar SRF T_B . **(Right)** Histogram of ΔT_B with respect to boxcar SRF T_B .

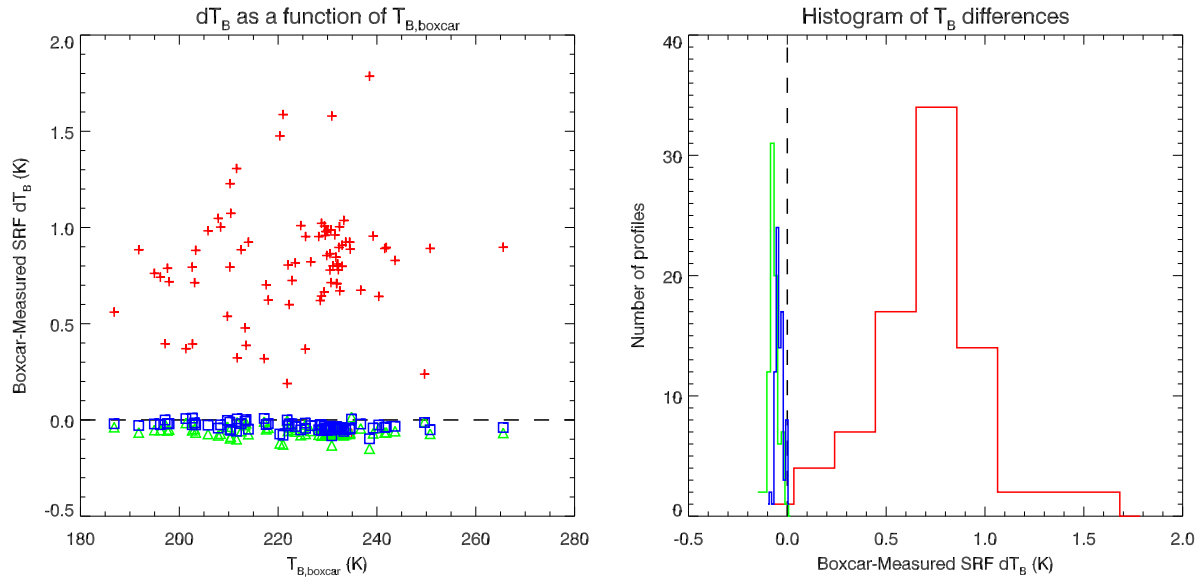


Figure B.13: NPP ATMS channel 13 calculated brightness temperature differences. **(Left)** ΔT_B as a function of the boxcar SRF T_B . **(Right)** Histogram of ΔT_B with respect to boxcar SRF T_B .

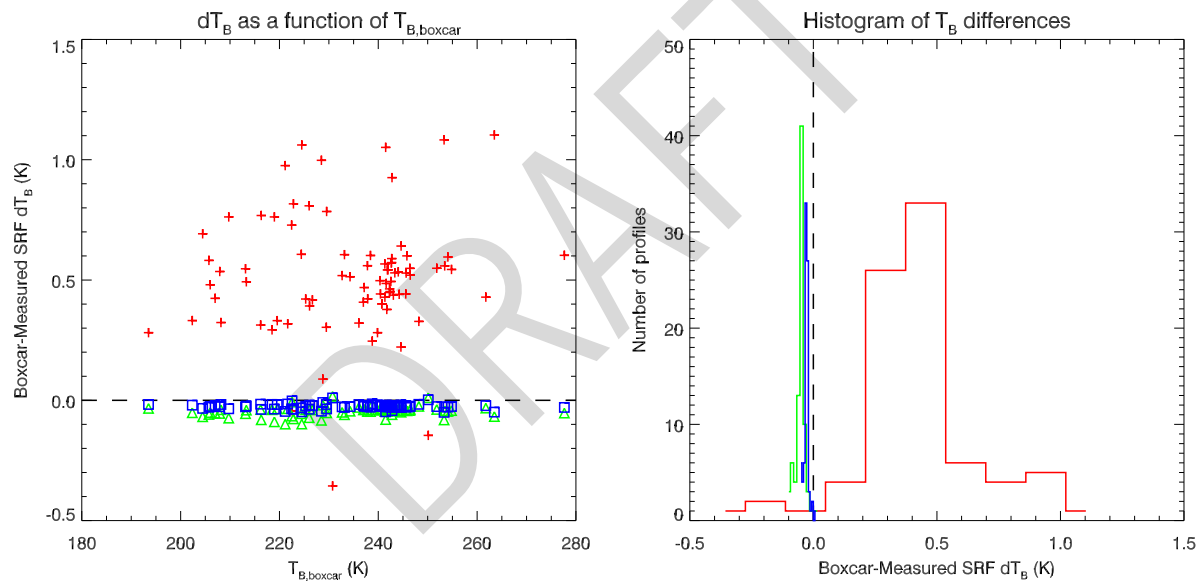


Figure B.14: NPP ATMS channel 14 calculated brightness temperature differences. **(Left)** ΔT_B as a function of the boxcar SRF T_B . **(Right)** Histogram of ΔT_B with respect to boxcar SRF T_B .

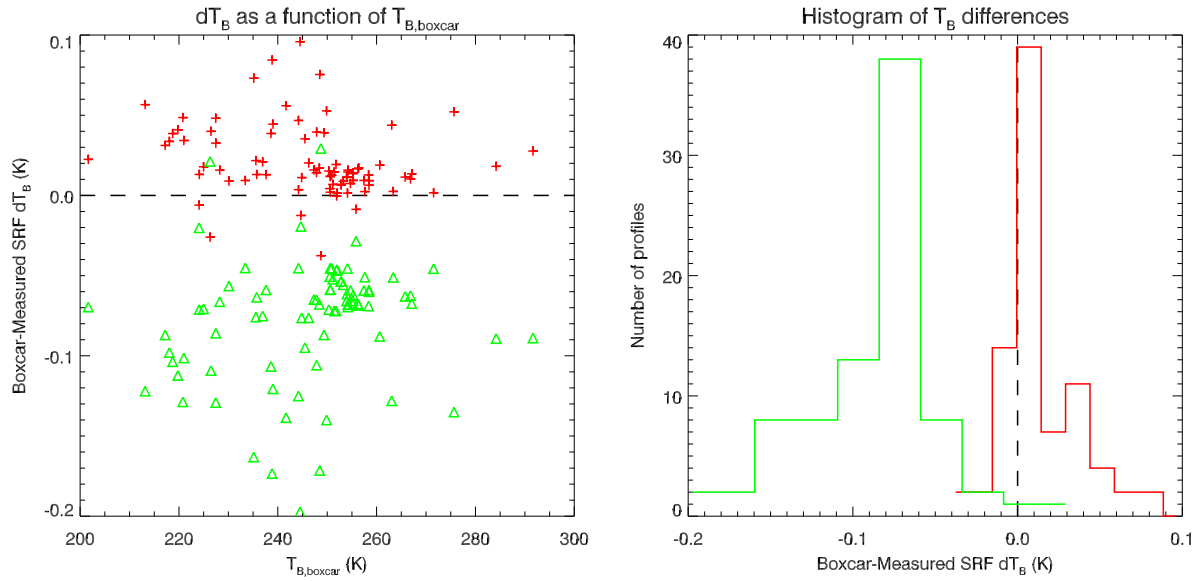


Figure B.15: NPP ATMS channel 15 calculated brightness temperature differences. **(Left)** ΔT_B as a function of the boxcar SRF T_B . **(Right)** Histogram of ΔT_B with respect to boxcar SRF T_B .

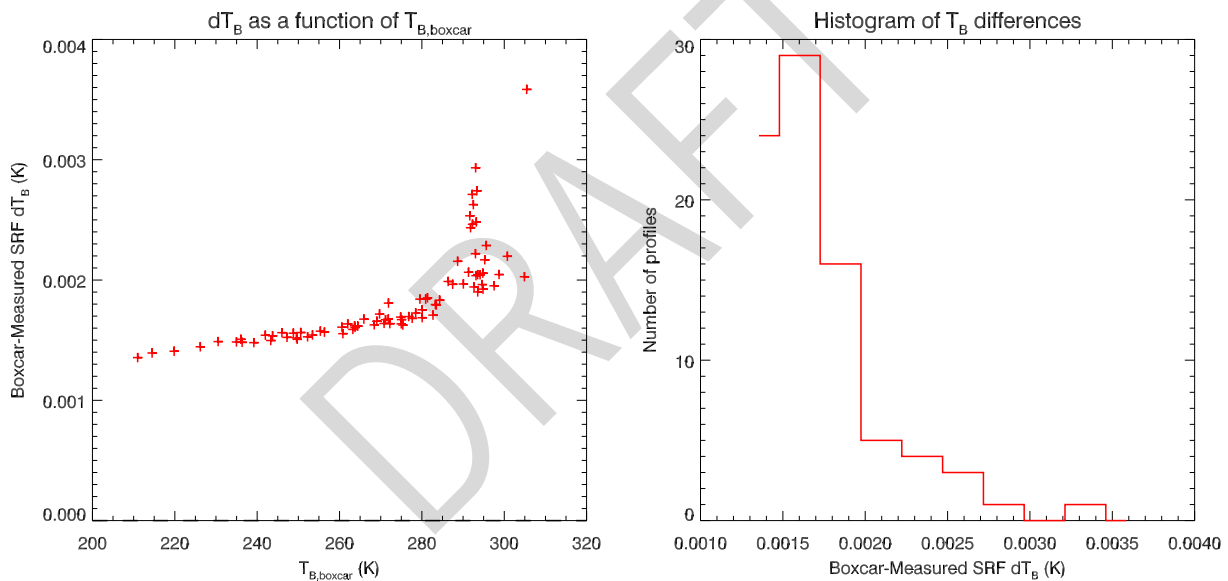


Figure B.16: NPP ATMS channel 16 calculated brightness temperature differences. **(Left)** ΔT_B as a function of the boxcar SRF T_B . **(Right)** Histogram of ΔT_B with respect to boxcar SRF T_B .

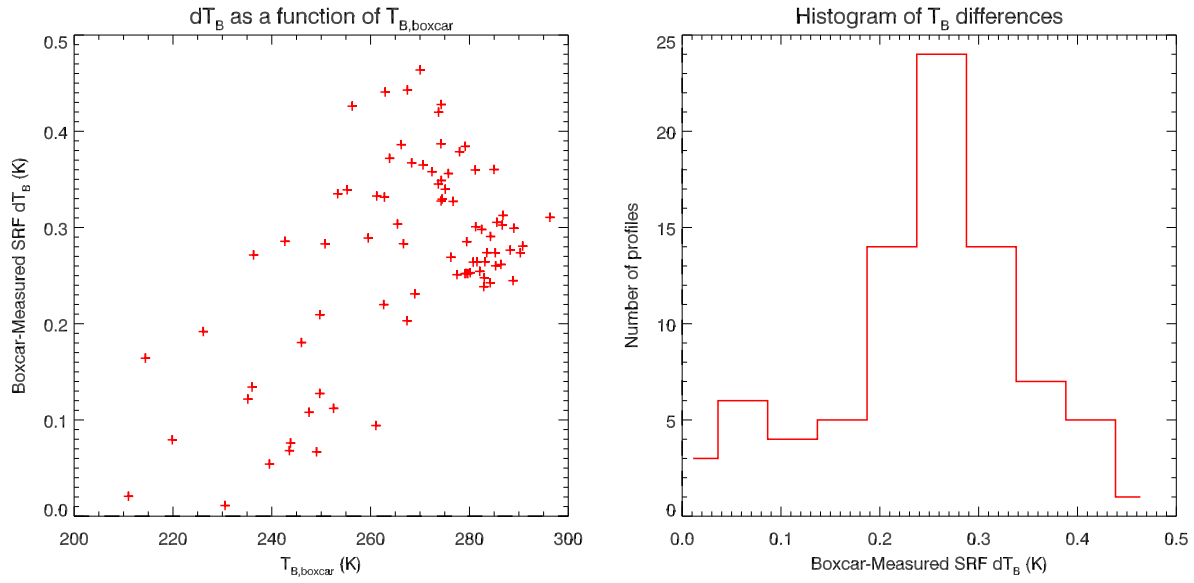


Figure B.17: NPP ATMS channel 17 calculated brightness temperature differences. **(Left)** ΔT_B as a function of the boxcar SRF T_B . **(Right)** Histogram of ΔT_B with respect to boxcar SRF T_B .

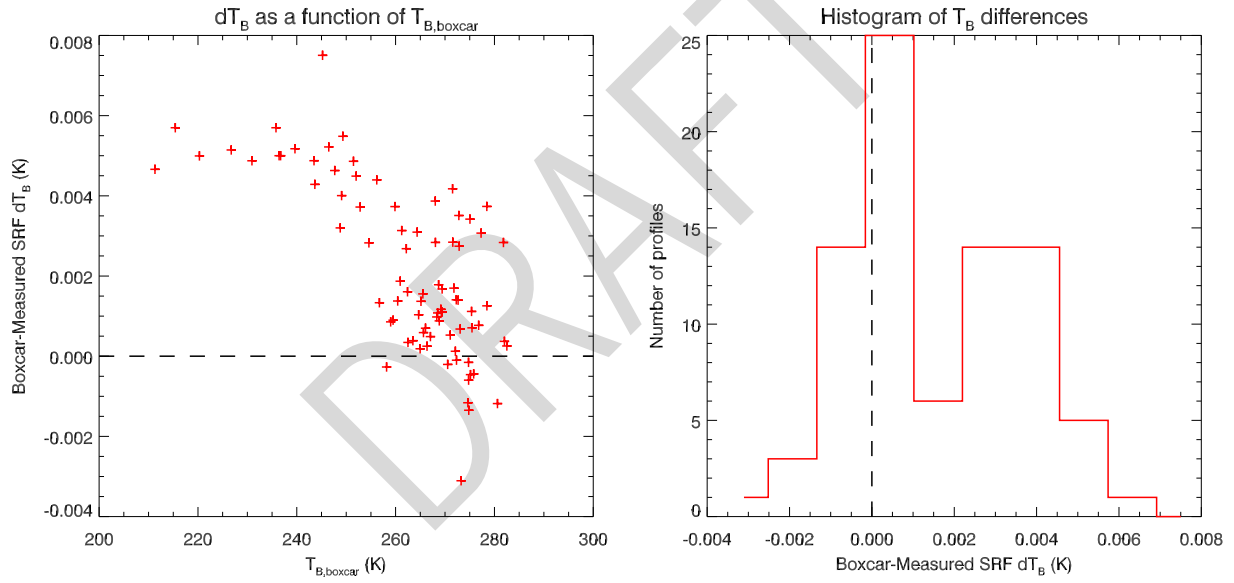


Figure B.18: NPP ATMS channel 18 calculated brightness temperature differences. **(Left)** ΔT_B as a function of the boxcar SRF T_B . **(Right)** Histogram of ΔT_B with respect to boxcar SRF T_B .

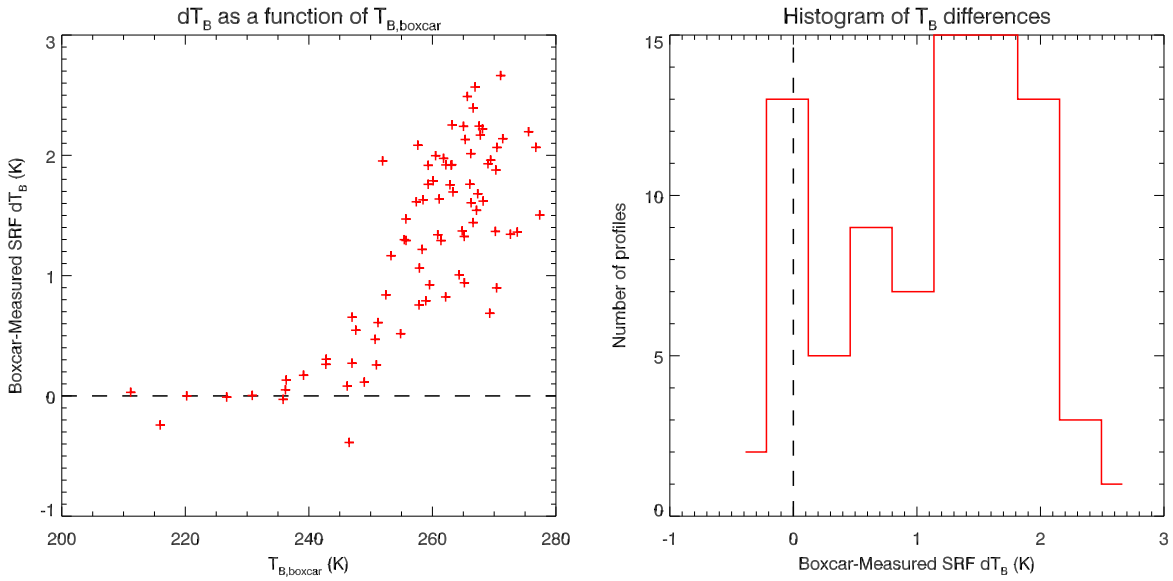


Figure B.19: NPP ATMS channel 19 calculated brightness temperature differences. **(Left)** ΔT_B as a function of the boxcar SRF T_B . **(Right)** Histogram of ΔT_B with respect to boxcar SRF T_B .

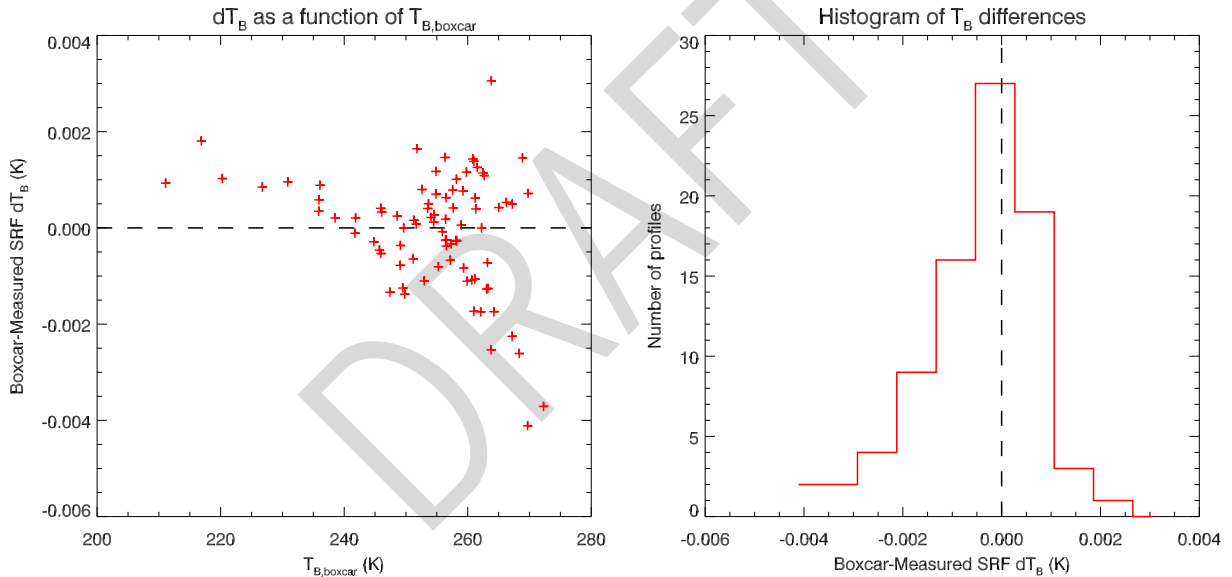


Figure B.20: NPP ATMS channel 20 calculated brightness temperature differences. **(Left)** ΔT_B as a function of the boxcar SRF T_B . **(Right)** Histogram of ΔT_B with respect to boxcar SRF T_B .

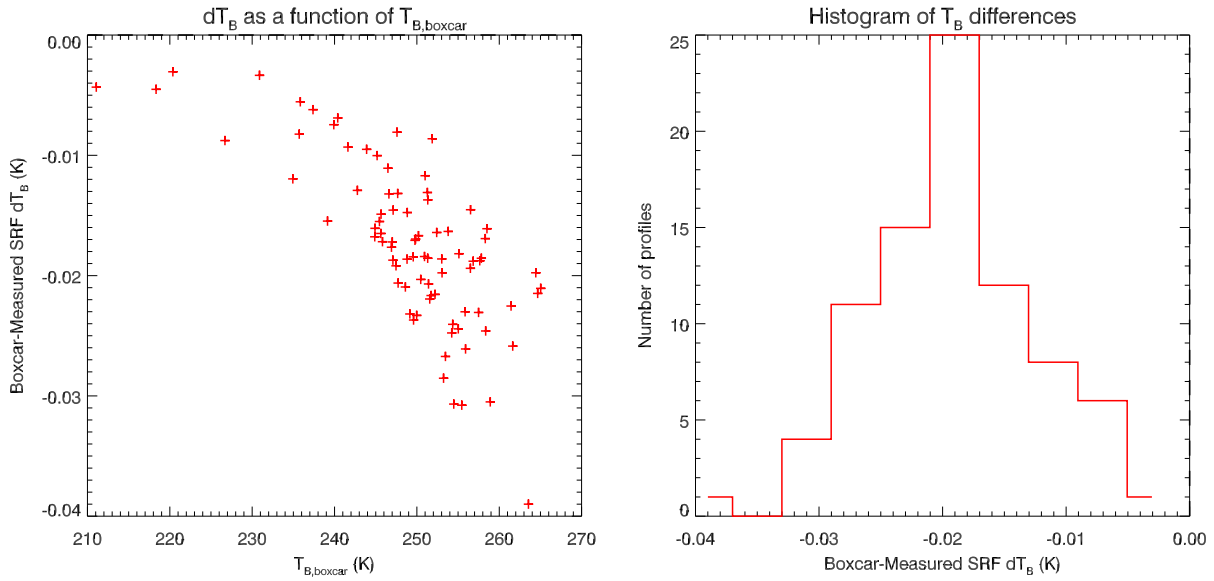


Figure B.21: NPP ATMS channel 21 calculated brightness temperature differences. **(Left)** ΔT_B as a function of the boxcar SRF T_B . **(Right)** Histogram of ΔT_B with respect to boxcar SRF T_B .

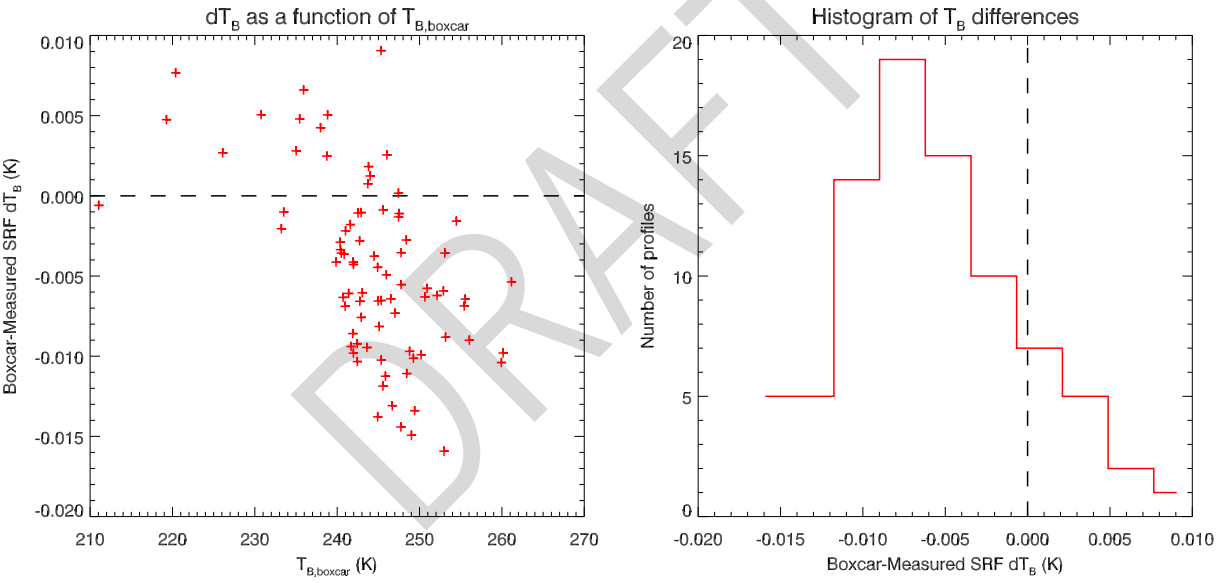


Figure B.22: NPP ATMS channel 22 calculated brightness temperature differences. **(Left)** ΔT_B as a function of the boxcar SRF T_B . **(Right)** Histogram of ΔT_B with respect to boxcar SRF T_B .